

1 Controls on Greenland moulin geometry and evolution from the

2 Moulin Shape model

3 Lauren C. Andrews¹, Kristin Poinar^{2,3}, Celia Trunz⁴

4 ¹Global Modeling and Assimilation Office, NASA Goddard Space Flight Center, Greenbelt, MD, 20771, USA

5 ²Department of Geology, University at Buffalo, Buffalo, NY, 14260, USA

6 ³Research and Education in eNergy, Environment and Water (RENEW) Program, University at Buffalo, Buffalo, NY, 14260,
7 USA

8 ⁴Geosciences Department, University of Arkansas, Fayetteville, AR, 72701, USA

9 **Correspondence:** Lauren C. Andrews (lauren.c.andrews@nasa.gov)

10 **Abstract.** Nearly all meltwater from glaciers and ice sheets is routed englacially through moulins. Therefore, the geometry
11 and evolution of moulins has the potential to influence subglacial water pressure variations, ice motion, and the runoff
12 hydrograph delivered to the ocean. We develop the *Moulin Shape* (MouSh) model, a time-evolving model of moulin geometry.
13 MouSh models ice deformation around a moulin using both viscous and elastic rheologies and models melting within the
14 moulin through heat dissipation from turbulent water flow, both above and below the water line. We force MouSh with
15 idealized and realistic surface melt inputs. Our results show that variations in surface melt change the geometry of a moulin
16 by approximately 20% daily and by over 100% seasonally. These size variations cause observable differences in moulin water
17 storage capacity, moulin water levels, and subglacial channel size compared to a static, cylindrical moulin. Our results suggest
18 that moulins are important storage reservoirs for meltwater, with storage capacity and water levels varying over multiple
19 timescales. Representing moulin geometry within subglacial hydrologic models would therefore improve the representation of
20 subglacial pressures, especially over seasonal periods or in regions where overburden pressures are high.

21 1 Introduction

22 Surface-sourced meltwater delivered to the glacier bed drives the evolution of the subglacial hydrologic system and associated
23 subglacial pressures (e.g., Iken and Bindshadler, 1986; Müller and Iken, 1973) The efficiency of the subglacial system, in
24 turn, changes the flow patterns of the overlying ice on daily, seasonal, and multi-annual timescales (e.g., Hoffman et al., 2011;
25 Iken and Bindshadler, 1986; Moon et al., 2014; Tedstone et al., 2015; Williams et al., 2020). Thus, glacial hydrology is a
26 crucial factor in short-term changes to glacier and ice sheet dynamics (Bell, 2008; Flowers, 2018).

27 On the Greenland Ice Sheet, surface meltwater can take multiple paths, depending on its origin location. In the
28 accumulation zone, meltwater may percolate through snow and firn, remaining liquid (Forster et al., 2014) or refreezing
29 (MacFerrin et al., 2019). In the ablation zone, meltwater runs over bare ice, coalesces into supraglacial streams, and pools into

30 supraglacial lakes (e.g., Smith et al., 2015). These surficial water features – rivers, streams, lakes, aquifers, etc. – direct
31 meltwater into englacial features that can deliver the water to the bed of the ice sheet (Andrews et al., 2014; Das et al., 2008;
32 Miège et al., 2016; Poinar et al., 2017; Smith et al., 2015). Englacial features include moulins, which are near-vertical shafts
33 with large surface catchments ($\sim 1\text{--}5\text{ km}^2$ per moulin, Banwell et al., 2016; Colgan and Steffen, 2009; Yang and Smith, 2016),
34 and crevasses, which are linear features with limited local catchments ($\sim 0.05\text{ km}^2$ per crevasse, Poinar et al., 2017). Together,
35 moulins and crevasses constitute a substantial fraction of the englacial hydrologic system.

36 Water fluxes through the englacial system, and therefore to the subglacial system, are non-uniform in space and time.
37 Quantifying these temporal variations in water fluxes to the glacier bed requires understanding the time evolution of the
38 supraglacial and englacial water systems that deliver it. Ongoing research is making great strides in characterizing the
39 supraglacial water network (Germain and Moorman, 2019; Smith et al., 2017; Yang et al., 2016). For instance, field
40 observations from Greenland indicate that much of the supraglacial water network terminates into crevasses and moulins
41 (McGrath et al., 2011; Smith et al., 2015) and that moulins are important modulators of surface melt inputs to the ice sheet bed
42 (Andrews et al., 2014; Cowton et al., 2013; Mejia et al., 2021).

43 Our knowledge of moulin sizes, scales, and time evolution has largely been informed by exploration and mapping of
44 the top tens to hundred meters of a few moulins (Benn et al., 2017; Covington et al., 2020; Gulley et al., 2009; Holmlund,
45 1988; Moreau, 2009). These sparse field data indicate that moulin shapes deviate greatly from simple cylinders. Furthermore,
46 deployments of tethered sensors into Greenland moulins have encountered irregularities including apparent ledges and plunge
47 pools (Andrews et al., 2014; Covington et al., 2020; Cowton et al., 2013), and seismic (Röösli et al., 2016) and radar (Catania
48 et al., 2008) studies suggest constrictions below the depths of human exploration. These direct near-surface and indirect deep
49 observations suggest that moulin geometry evolves a high degree of complexity at all depths.

50 State-of-the-art subglacial hydrology models are forced by meltwater inputs that enter the system through crevasses
51 or moulins. These models generally represent the geometry of moulins in a simplified and time-independent manner, for
52 instance as a static vertical cylinder (e.g., Hewitt, 2013; Hoffman et al., 2016; Werder et al., 2013) or cone (Clarke, 1996;
53 Flowers and Clarke, 2002; Werder et al., 2010). The basis for the cylindrical simplification arises from the assumption that
54 depth-dependent variations in moulin size are small relative to the vertical scale of the moulin. The basis for time independence
55 is the assumption that the moulin capacity is, again, small relative to that of the subglacial system. However, neither of these
56 assumptions have been tested. Here, we explore the extent to which time evolution of moulin geometry affects the rate of
57 subglacial meltwater input and subglacial pressure in channelized regions of the bed.

58 We present the Moulin Shape (MouSh) model, a new, physically based numeric model that evolves moulin geometry
59 over diurnal and seasonal periods. The MouSh model can be coupled to subglacial hydrology models to more completely
60 characterize the time evolution of the englacial and subglacial hydrologic systems, which are intimately linked.

61 2 Moulin physical model

62 We develop the Moulin Shape (MouSh) model, a numeric model of moulin evolution that considers ice deformation and ice
63 melt associated with the dissipation of energy from turbulently flowing meltwater (Fig. 1). We include here a detailed
64 description of the model framework and each module that influences the time-evolving geometry of the modeled moulin (Fig.
65 2a).

66 2.1 Moulin geometry coordinate system

67 We discretize our model in the vertical (z) and radial (r_1 and r_2) directions, treating the moulin as a stack of egg-shaped (semi-
68 circular, semi-elliptical) holes in the ice that both change in size and move laterally relative to each other. We calculate moulin
69 geometry (elliptical radii r_1 and r_2) and water level (h_w) with a 5-minute timestep dt . Model calculations are performed in
70 cylindrical coordinates, where $\Pi(z)$ is the perimeter of the semi-circular, semi-elliptical moulin, using Ramanujan's
71 approximation:

$$72 \quad \Pi \approx \pi r_1 + \frac{1}{2} \pi [3(r_1 + r_2) - \sqrt{(3r_1 + r_2)(r_1 + 3r_2)}] \quad (1)$$

73 Here, r_1 and r_2 are the minor and major radii, respectively, for each node in the vertical direction. The minor radius r_1 is also
74 the radius of the half-circle.

75 We calculate the cross-sectional area of the semi-circular, semi-elliptical moulin as follows:

$$76 \quad A_m = \frac{\pi r_1}{2} (r_2 + r_1) \quad (2)$$

77 The plan-view orientation of the radii and the coordinate system, as detailed on a remotely sensed moulin, are indicated in
78 Fig. 2b-d. The elliptical shape was chosen to reflect the observation that supraglacial meltwater flows into a moulin along a
79 single side above the water line. This asymmetry leads to a nonuniform, noncircular geometry above the water level, which
80 can affect the total amount and evolution of water storage at high water levels. This choice is in line with observations of a
81 Greenland moulin becoming more elliptical over time (Rössli et al., 2016). For simplicity, MouSh contains an option to set
82 the moulin cross-sectional geometry to a circle, rather than an egg (see Supplement S2).

83 Each module is also dependent on the depth varying hydrostatic and cryostatic pressures. We subtract the cryostatic
84 pressure, P_i , from the hydrostatic pressure, P_w , to get the total depth-dependent effective pressure N at all levels z within the
85 moulin:

$$86 \quad P_i = \rho_i g (H_i - b) \quad (3a)$$

$$87 \quad P_w = \rho_w g (h_w - b) \quad (3b)$$

$$88 \quad N = P_w - P_i \quad (3c)$$

89 where H_i is the ice thickness; h_w is the height of the water above the bed; z is the vertical coordinate; ρ_i and ρ_w are ice and
90 water density, respectively; and g is gravitational acceleration (Table 1). In this formulation, positive pressures causes
91 outward expansion of the moulin walls (radial growth), and negative pressures reduces the size of the moulin (radial closure).

92 We use a flat bed at sea level for all model runs presented here, so bed elevation $b = 0$.

94 2.2 Ice deformation modules

95 We represent the deformation of the ice with the simplest possible combination of elastic and viscous components: a Maxwell
 96 rheology, where elastic and viscous deformation occur independently, without interaction (Turcotte and Schubert, 2002). The
 97 Maxwell model comprises an elastic element (a spring) and a viscous element (a dashpot) in series and is standard in
 98 geophysical modeling. The response timescale in our Maxwell model is equal to $(E \times A \times \tau^2)^{-1}$ where E is Young's modulus,
 99 A is the viscous flow law parameter, and τ is stress (Turcotte and Schubert, 2002). The Maxwell timescale is thus roughly 10–
 100 100 hours for typical Greenland ice. On timescales shorter than the Maxwell timescale, ice deformation is primarily elastic.
 101 On longer timescales, viscous deformation dominates.

102 Elastic deformation is described in Sect. 2.2.1. We represent total viscous deformation in two modes: (1) radial
 103 opening and closure of the moulin, which changes the size of the moulin (Sect. 2.2.2), and (2) vertical shear of the moulin,
 104 which changes the shape but not the size of the moulin (Sect. 2.2.3).

105 2.2.1 Elastic deformation

106 Field measurements indicate that, nearly universally during the melt season, the water level in a moulin varies at a sub-hourly
 107 timescale (Andrews et al., 2014; Covington et al., 2020; Cowton et al., 2013; Iken, 1972). This variability is shorter than, but
 108 comparable to, the Maxwell timescale for ice (10–100 hours; see Sect. 2.2); therefore, we must assume that elastic deformation
 109 plays a role in the response of the ice to variations in moulin water level.

110 Weertman (1971, 1973, 1996) applied dislocation fracture mechanics principles to vertical glaciological features:
 111 water-filled crevasses. These equations have been applied to supraglacial lake drainages (Krawczynski et al., 2009) and slow ice
 112 hydrofracture (Poinar et al., 2017). However, these problems are Cartesian (linear), not cylindrical, so their solutions are not
 113 readily adaptable to a moulin. The stress and deformational patterns around cylindrical boreholes have been well studied in
 114 the rock mechanics literature (Amadei, 1983; Goodman, 1989; Priest, 1993). We therefore base our description of the stress
 115 field surrounding the moulin on that of a fluid-filled borehole in a porous rock medium, described by Aadnøy (1987) and based
 116 on the Kirsch equations, which describe stresses surrounding a circular hole in a rigid plate (Kirsch, 1898). We assume plane
 117 strain and approximate our moulin as a stack of such plates with analogous holes (Goodman, 1989). A subtle difference is that
 118 our moulin shape is not circular, but egg-shaped: half circular, half elliptical.

119 At each vertical level z in the moulin, we apply Hooke's Law to the stress field to calculate the strain, in horizontal
 120 cross-section, at all points on the moulin wall and in the surrounding ice for both radii r_l and r_2 . We then integrate these strains
 121 from an infinite distance (cylindrical coordinate $r = \infty$) to the moulin wall ($r_l, r_2 = r_m$). A full derivation, based on the stress
 122 states in a borehole described by Aadnøy (1987), is in Supplement S1. We express the total radial elastic deformation r_e of a
 123 moulin segment as:

$$r_e = \frac{r_m}{E} \left[(1 + \nu) \left(N - \frac{1}{2}(\sigma_x + \sigma_y) \right) + \frac{1}{4}(\sigma_x - \sigma_y)(1 - 3\nu - 4\nu^2) + \frac{1}{4}\tau_{xy}(2 - 3\nu - 8\nu^2) \right] \quad (4)$$

Here, E is Young's modulus for uniaxial deformation, ν is Poisson's ratio, and σ_x , σ_y , and τ_{xy} are the background deviatoric and shear stresses that describe the regional setting of the moulin (typically compressive and of order 100 kPa; Poinar and Andrews, 2021). The model is designed to accept user-defined deviatoric and shear stresses; we choose values $\sigma_x = 0 \text{ kPa}$, $\sigma_y = 50 \text{ kPa}$, and $\tau_{xy} = -50 \text{ kPa}$. However, because the deviatoric and shear stresses are poorly constrained, we also test the simplification $\sigma_x = \sigma_y = \tau_{xy} = 0$ (Supplement S2), which simplifies the elastic deformation r_e :

$$r_e = \frac{r_m}{E} (1 + \nu) N \quad (5)$$

Unlike viscous deformation and melting, elastic deformation is instantaneous. However, we take advantage of the observation that elastic deformation is driven by changes in the cryostatic and hydrostatic pressures. Therefore, we express Eq. 4 and Eq 5 as an elastic 'deformation rate' for non-zero (Eq 6a) and zero (Eq 6b) stresses:

$$dr_e = \frac{1}{E} \left(r_m (1 + \nu) \frac{dN}{dt} + \left[(1 + \nu) \left(N - \frac{1}{2}(\sigma_x + \sigma_y) \right) + \frac{1}{4}(\sigma_x - \sigma_y)(1 - 3\nu - 4\nu^2) + \frac{1}{4}\tau_{xy}(2 - 3\nu - 8\nu^2) \right] \frac{dr_m}{dt} \right) dt \quad (6)$$

$$dr_e = \frac{(1 + \nu)}{E} \left(r_m \frac{dN}{dt} + N \frac{dr_m}{dt} \right) dt \quad (7)$$

Equations 6 and 7 assume that both effective pressure and moulin radius vary smoothly over the time interval in question, which is generally true for small timesteps (5-minutes in our model). We apply Eq. 6 or 7 to both moulin radii, the semi-circular radius r_l and the semi-elliptical major radius r_2 , separately. When water is above the flotation level, elastic deformation opens the moulin at all depths below the water line. When the water level is below flotation, which is the typical case, elastic deformation closes the moulin at all depths. The values of the surface stresses σ_x , σ_y , and τ_{xy} determine the sign of the deformation above the water line.

2.2.2 Viscous radial opening and closure

Moulins close when they lose their water source at the end of a melt season (Catania and Neumann, 2010). Similarly, boreholes close if they are not filled with drilling fluid with a density similar to ice (Alley, 1992). Our modeled moulin is intermediate to these edge cases because it typically contains water. When the moulin is filled with water to the flotation level, it will stay open at its base and viscously close at and below the water level. When the water level is above flotation, the moulin will viscously open in regions where hydrostatic pressure exceeds the cryostatic pressure. When the water level is below flotation, which is the typical case, viscous deformation shrinks the moulin at all depths.

We calculate strain rate ($\dot{\epsilon}$) from the total depth-dependent effective pressure N (Eq. 3c) using Glen's Flow Law:

$$\dot{\epsilon} = F_* A(T_i, P_i) \cdot \left(\frac{1}{3} N \right)^n \quad (8)$$

where F_* is the flow law enhancement factor, and $A(T_i, P_i)$ is the flow law parameter. For the flow law parameter, we use the standard relationship from Cuffey and Paterson (2010, Eq. 3.35), which is a function of ice temperature T_i and ice pressure P_i .

We follow borehole studies by Naruse et al (1988) and Paterson (1977) to write strain, ε , in the radial direction as

$$\varepsilon = \ln\left(\frac{r_f}{r_0}\right) \quad (9)$$

where a moulin with initial radius r_0 and final radius r_f underwent radial strain of ε .

We use the time derivative of Eq. (9) to calculate the change in moulin radius due to viscous deformation:

$$dr_v = r_m \exp(\dot{\varepsilon} dt) - r_m \quad (10)$$

with strain rate given by Eq. (8). This is the same relationship used by Catania and Neumann (2010).

2.2.3 Shear deformation

We use Glen's Flow Law to calculate the change in shape of the moulin due to regional-scale ice flow. This deforms the entire moulin in bulk, shearing it in the vertical and shifting it laterally downstream, without changing its radii. Basal sliding is not currently included in the model. To represent deformation, we discretize the moulin as a stack of plates with elliptical (or circular) holes with a thickness dz and represent deformational ice flow as displacement between these plates.

We calculate the rate of deformational ice flow u_d in the downstream direction from ice temperature T and pressure N , surface slope α , a constant enhancement factor F_* , and ice thickness H_i , using Glen's Flow Law (Cuffey and Paterson, 2010):

$$u_d = 2F_*(\rho_i g \alpha)^n \cdot \int_b^{H_i} A(T_i, P_i)(H_i - z)^n dz \quad (11)$$

We obtain ice deformation rates of $\sim 20 \text{ m yr}^{-1}$, which is typical of the ablation zone in western Greenland (Ryser et al., 2014).

2.3 Phase change modules

The second mode that changes the geometry of the moulin is ice ablation from or accretion to the moulin walls. During the melt season, the flow of water into and through the moulin generates turbulence, which as it dissipates acts to melt back the moulin walls, expanding the size of the moulin. There is also a small component of melting due to temperature differences between the water and surrounding ice. Outside the melt season, conduction of latent heat into the surrounding ice causes stagnant water to freeze back onto the moulin walls, contracting the size of the moulin.

2.3.1 Refreezing

Refreezing occurs in cold ice when water flow is absent or slow enough that the rate of heat conduction into the surrounding ice drops the water temperature to the freezing point. These conditions occur primarily outside the melt season. When these conditions are met, we apply a radial freezing term, which is parameterized economically, following Alley (2005):

$$dr_f = 2 \frac{T_i - T_{mp}}{L_f} \sqrt{\frac{k_i C_p}{\pi \rho_i}} (\sqrt{t_t} - \sqrt{t_t - dt}) \quad (12)$$

Here, $T_i - T_{mp}$ is the depth-varying difference between the far-field temperature (prescribed as from borehole temperature observations) and the moulin water temperature, which is taken as the pressure melting temperature T_{mp} . C_p is the specific

83 heat capacity of ice. The refreezing rates thus evolve exclusively based on the elapsed time since the cessation of turbulent
 84 flow, t_t .

85 We calculate the change in moulin water volume from freezing, V_{fz} , by summing the refrozen ice thickness in a
 86 timestep, dr_f , around the perimeter of the moulin at all depths z , and converting ice volume to water volume:

$$87 \quad V_{fz} = \frac{\rho_i}{\rho_w} \int_b^{h_w} \Pi(z) r_f(z) dz \quad (13).$$

88 2.3.2 Moulin wall melting

89 During the melt season, turbulent energy dissipation from water flowing through the moulin melts back the moulin walls. The
 90 dissipation of turbulent energy and the associated melting of the surrounding ice will increase the local moulin radius. We
 91 parameterize turbulence in two separate spatial domains: (1) within the water column of the moulin, where r_1 and r_2 are evolved
 92 uniformly, and (2) above the water level along the side of the moulin, as supraglacial input falls to the water level, where only
 93 r_2 is evolved.

94 The parameterizations of turbulently driven melting we use in both regimes rely on three simplifications. First, the
 95 volume of water moving through each vertical model node is constant within each time step. This ensures that water mass is
 96 conserved and that all model elements below the water line are water filled; however, this eliminates the potential long-term
 97 storage of meltwater within plunge pools caused by non-uniform incision into the ice. Second, all energy generated from
 98 turbulent dissipation is instantaneously applied to melting the surrounding ice. This neglects any heat transport within the
 99 water, which is a common approximation in subglacial models (e.g., Hewitt, 2013; Schoof, 2010; Werder et al., 2013). Third,
 00 we also make the simplifying assumption that meltwater entering the moulin is at 0°C and at the pressure melting temperature
 01 T_{mp} at all points below the water line, though we do not model the impact of this temperature change on melting because
 02 moulin water temperatures are unknown.

03
 04 *Submerged zone:* Below the water line, the vertical velocity of the water is dictated by the hydraulic gradient within the system
 05 and the local cross-sectional area of the moulin. Under such conditions, head loss – the departure of the hydraulic head from
 06 that calculated by Bernoulli’s equation – reflects the energy dissipated as heat. We parameterize head loss using the Darcy–
 07 Weisbach equation, which relates water velocity u_w to changes in the hydraulic gradient dh_w/dl (head loss per unit length along
 08 flow), via the hydraulic radius R_h and a dimensionless friction factor f . Because water velocity is constrained by mass balance
 09 within the system, we calculate the head loss dh_w/dl as follows:

$$10 \quad \frac{dh_w}{dl} = \frac{u_w^2 f}{8 R_h g} \quad (14)$$

11 The differential element dl represents the path length over which the water experiences head loss: $\partial l = \sqrt{\partial x^2 + \partial z^2}$ for
 12 horizontal distance dx and vertical drop dz . The friction factor f is a unitless model parameter that controls the rate of head loss
 13 within the system. Its value thus directly affects the amount of melting. Most subglacial models fix the Darcy–Weisbach
 14 friction factor, with values ranging from 0.01 to 0.5 (e.g., Colgan et al., 2011b; Schoof, 2010; Spring and Hutter, 1981) or use

equivalent values of Manning’s n (e.g., Hewitt, 2013; Hoffman and Price, 2014). Alternatively, other models parameterize channel roughness using a geometry-dependent friction factor (e.g., Boulton et al., 2007; Clarke, 2003; Flowers, 2008). Thus, MouSh has options for fixed or variable f .

The friction factor within the submerged zone is indicated by f_m and in the open channel zone by f_{oc} . To explore the impact of the chosen friction factor, we complete a sensitivity study (Sect. 2.3 and 3.2) where we vary the friction factor in water filled sections, f_m , over an expected range, centered on $f_m = 0.1$. We use a constant $f_m = 0.1$ for all other model runs presented.

Because we approximate the moulin as a half-circular, half-elliptical cylinder with perimeter Π , the hydraulic radius R_h of a water filled node is:

$$R_h = \frac{A_m}{\Pi} \quad (16).$$

To calculate moulin wall melting, we use a simple energy balance equation, following previous work (e.g., Gulley et al., 2014; Jarosch and Gudmundsson, 2012; Nossokoff, 2013):

$$\rho_i C_w (T_{pmp} - T_i) \frac{dA_m}{dt} + \rho_i L_f \frac{dA_m}{dt} = Q \left(\rho_w g \frac{dh_w}{dl} \right) \quad (17)$$

The first term represents the energy needed to warm the surrounding ice to the pressure melting temperature of water T_{pmp} .

Equation (17) can be rearranged and combined with equation (14) to provide the area of ice melted:

$$dA_t = Q_{out} \left(\rho_w g \frac{u_w^2 f}{4 R_h g} \right) \left(\rho_i C_w (T_{pmp} - T_i) + \rho_i L_f \right)^{-1} dt \quad (18)$$

Where Q_{out} is the discharge from the moulin-subglacial system as dictated by the subglacial model component (Sect. 2.4.2); and $T_i - T_{pmp}$ is the temperature difference between the water (prescribed to be at the pressure melting point) and the surrounding ice, which we can vary from site to site around Greenland as described in Table 1. Note that Eq. 18 determines the area of ice that is removed through melting. For each time step, we reframe Eq. 18 into radial melting within an egg-shaped moulin using information about the previous geometry and the assumption that melting occurs uniformly around the perimeter:

$$dr_t = 2dA_t / [\pi(5r_1 + 3r_2 - \sqrt{(3r_1 + r_2)(r_1 + 3r_2)})] \quad (19).$$

Equation 19 is simplified when considering a circular geometry ($r_1 = r_2$).

Unsubmerged zone: Above the water line, a variety of complex processes drive melting. A first-principles approach would be to quantify melting due to the potential energy loss of falling water, following the work on terrestrial waterfalls (e.g., Scheingross and Lamb, 2017). However, nearly all waterfall-based parameterizations rely on abrasion between waterborne sediment and the substrate as the primary mechanism of erosion. Instead, we implement a simple parameterization for open-channel flow with the understanding that the complexities of thermal erosion are not completely captured. In our model, open-channel melting occurs only on the up-glacier wall of the moulin and follows two ad-hoc rules based on the slope between the vertical nodes: (1) open-channel turbulent melting is applied if the slope of the upstream moulin wall allows water to flow

over it; and (2) a small, prescribed amount of melting is applied when the upstream wall slope is vertical or overhung, because while water cannot flow directly along the ice, spray and other processes likely drive some amount of melting. These cases are respectively (1) the open-channel zone and (2) the falling water zone.

In the open-channel zone, we use a similar approach as for melting below the water line. However, the hydraulic radius R_h is adjusted to reflect the observation that water runs down only one wall of the moulin, and a higher friction factor is used to parameterize complex geometries. Due to the presence of a discontinuity between open-channel and water-filled regions (at the water line), we parameterize the hydraulic radius of open channel flow as $R_{hopen} = 0.5r_2$. We also use a higher open channel friction factor f_{oc} of 0.8 to parameterize observed extensive scalloping (e.g., Gully et al., 2014; Covington et al., 2020). We apply melting to only the elliptical side of the moulin, defined by r_2 derived using Eq. 18. Note that the hydraulic radius prescribed for open-channel flow is likely larger than the small region over which water is flowing in the natural system (Fig. 2a,d). Further, the resulting melt dA_{oc} is applied only to the major radius to calculate dr_{oc} .

In the falling water zone, there is very limited interaction between the moulin walls and the water. For simplicity, we assume that a small fraction, f_p , of the potential energy lost as water falls is deposited into the moulin walls, perhaps as the kinetic energy of spray. The change in radius due to this process is as follows:

$$dr_{mf} = f_p \frac{(\rho_w/\rho_i)gQ}{L_f\pi} dt \quad (20)$$

We set f_p to 0.1 for all model runs presented.

We add the volume of ice melted to the water already in the moulin, similarly to Eq. 12 for V_{fz} . We calculate the change in moulin water volume from melting by summing the melted ice thickness, r_{mf} , around the perimeter of the moulin at all depths z , and converting ice volume to water volume:

$$V_{wallmelt} = \frac{\rho_i}{\rho_w} dt \int_b^{H_i} \pi(z)r_{mf}(z) + A_{oc}(z) + A_t(z) dz \quad (21).$$

2.4 Water flux into and out of the moulin (Mass conservation)

Water balance within the moulin and the subglacial channel is dictated by recharge from a supraglacial stream (Q_{in} , Sect. 2.4.1), discharge through a subglacial channel (Q_{out} , Q_{base} ; Sect. 2.4.2) and any change in volume due to melting or refreezing, such that the volume of water in the system (V) is:

$$\frac{dV}{dt} = Q_{in} - Q_{out} + Q_{base} + \frac{(dV_{wallmelt} - dV_{frz})}{dt} \quad (22).$$

The integral term varies in space and time, with high melt rates above the water line during the melt season (when $Q_{in} > 0$), and moderate melt rates at and below the water line during and after the melt season, when there is water flow through the moulin ($Q_{out} > 0$) and refreezing below the water line throughout the winter (when $Q_{in} = Q_{out} = 0$). The MouSh model can also accept an additional prescribed base flow Q_{base} directly to the subglacial module. We design base flow as a loose approximation of additional subglacial water inputs from varied upstream sources, including other moulins on the same subglacial channel, regional basal melt, and the addition and removal of meltwater from subglacial storage. Base flow is

generally required to maintain realistic moulin water levels. In the moulin runs forced by realistic Q_{in} , we represent subglacial flow from ~5 surrounding moulins by prescribing base flow as five times the running 5-day mean of Q_{in} . In other model runs, we do not include base flow. The addition of base flow is designed to represent the widespread seasonal evolution of surface melt; its inclusion maintains a slightly larger subglacial channel than would otherwise occur, which reduces otherwise unrealistically large daily swings in modeled moulin water level.

2.4.1 Meltwater runoff from the ice-sheet surface

We force the MouSh model with time-varying water inputs from the supraglacial environment, Q_{in} . We use two different Q_{in} scenarios: a simple diurnal cosine with maximum and minimum discharges ranging between ~1 and 5 m³s⁻¹, in rough agreement with observations near the margins (Eq. 23, Chandler et al., 2013; McGrath et al., 2011; Smith et al., 2017); and realistic supraglacial discharge over a melt season, determined by using in-situ surface melting data and internally drained catchment size and geometry (Yang and Smith, 2016).

We use the following cosine curve to represent our simplest form of supraglacial discharge into the moulin during sensitivity studies:

$$Q_{in} = \cos(\pi(t - 19.5)/12) + 3 \quad (23)$$

Here, t is time in hours and Q_{in} is in m³ s⁻¹. This function has its daily peak at 19:30 hours and a daily minimum at 07:30.

To examine a set of realistic moulins, we select three supraglacial basins from Yang and Smith (2016) and derive their size, distance from terminus from information provided therein (Basin 1-3; Table 2). We derive surface runoff from MERRA-2 reanalysis (Gelaro et al., 2017; Smith et al., 2017). Surface runoff values for the 2019 melt season were modified using a synthetic unit hydrograph derived for the ablation zone and parameters appropriate for western Greenland (Table 2, Smith et al., 2017). The use of a unit hydrograph parameterizes the time and magnitude adjustments expected from meltwater routing over the ice surface. The parameters for the unit hydrograph were determined during the middle of the melt season and therefore may inaccurately represent routing delays at the beginning and end of the melt season. Further details on supraglacial and internal catchment characteristics are included in Sect. 2.5.2.

2.4.2 Water flow from the subglacial system

We couple the moulin model and a single evolving subglacial channel controlled by melt opening and creep closure (Covington et al., 2020; Schoof, 2010) using a reservoir-constriction model (Covington et al., 2012) that simulate flows between the moulin and subglacial channel. Following Covington et al. (2020), the rate of change of moulin water level h_w is

$$\frac{dh_w}{dt} = \frac{1}{A_m(h_w)} \frac{\partial V}{\partial t} \quad (24)$$

With the change in water volume within the system being dV and the volume of the moulin-subglacial system is related to the channel S and the moulin cross-sectional area A_m . The water volume is related to Q_{in} , Q_{base} and Q_{out} , where Q_{out} is the meltwater output from the subglacial channel, defined as follows:

$$Q_{out} = c_3 S^{5/4} \Psi / \sqrt{|\Psi|} \quad (25)$$

Here, S is the subglacial channel cross-sectional area. The hydraulic gradient $\Psi = -\rho_i g \frac{d(h_w - b)}{dL}$ is a linear gradient in h_w to the outlet at a horizontal distance L , where the pressure head is zero. In our calculations, the bed elevation b is zero. Finally, c_3 is a flux parameter:

$$c_3 = \frac{2^{5/4}}{\pi^{1/4}} \sqrt{\frac{\pi}{(\pi+2)\rho_w f}}. \quad (26)$$

Equation (26) for c_3 follows Covington et al. (2020), who corrected a small error from the original Schoof (2010) formulation.

We use an equation from Schoof (2010) for the time rate of change in subglacial channel cross-section area S , with the first part describing the turbulent melting of the subglacial channel walls, and the second term describing closure due to the pressure of the overlying ice:

$$dS = (c_1 Q_{out} \Psi - c_2 N^n S) dt \quad (27)$$

Here, the constant $c_1 = \frac{1}{\rho_i L_f}$ with ρ_i the ice density and L_f the latent heat fusion of ice, the constant $c_2 = 2A(T_i, N)n^{-n}$ with the Glen's flow law parameters for the subglacial component defined as $A = 6 \cdot 10^{-24} \text{Pa}^{-3} \text{s}^{-1}$.

Replacing Q_{out} , Ψ , and N in Eq. (27) yields

$$dS = c_1 c_3 S^{5/4} \left(\frac{\rho_w g h_w}{L} \right)^{3/2} - c_2 (P_i - \rho_w g h_w)^n S) dt \quad (28)$$

Equations (24) and (28) are numerically solved simultaneously, as in Schoof (2010) and Covington et al. (2021). The parameters used in this module are included in Table 1 and are the same as those used in the englacial component of MouSh, apart from the flow law parameter A . In the englacial system, A is calculated from local temperature within the ice column, which can be as cold as -23°C in western Greenland (Iken et al., 1993). This contrasts with the temperature at the ice-bed interface, which must be at the melting point; thus, the subglacial component of MouSh uses a higher fixed A value.

In its current configuration, the subglacial module provides a single set of outputs representative of conditions at the moulin. This is primarily because this study focuses on the evolution of a moulin and is not representative of a channel running from a moulin to the terminus in a natural system. A more complex subglacial model would more accurately resolve the spatial changes in subglacial channel geometry and flow.

2.5 Suites of model experiments

To examine the sensitivity of the MouSh model to uncertain parameters, ice and meltwater characteristics, and model choices, and difference from previous moulin parameterizations, we run four suites of experiments. While these experiments do not cover the complete range of possibilities, they were designed to address primary uncertainties in the MouSh model and examine how moulin geometry might vary spatially and temporally.

2.5.1 Quasi-equilibrium and the impact of diurnal supraglacial variability

Under steadily varying conditions such as a repeating diurnal variation, the modeled moulin reaches a quasi-equilibrium state independent of initial conditions with melting opposing viscous and elastic deformation and the only change being driven by shear deformation. We examine the quasi-equilibrium state and the impact of supraglacial variability on this state. Supraglacial runoff Q_{in} is highly variable with seasonal, event, and diurnal variability in surface melting modified by supraglacial drainage basin characteristics as it is routed to a moulin. Moulin water level and shape respond to these patterns of variability. To examine the impact of Q_{in} magnitude (mean) and Q_{in} amplitude (variability), we perform a series of model runs that vary the magnitude of a cosine curve between 1 and 20 m^3s^{-1} with a fixed amplitude of 0.5 m^3s^{-1} and a series of runs that vary the amplitude of a cosine curve between 0 and 2 m^3s^{-1} with a fixed magnitude of 5.0 m^3s^{-1} . The amplitude as one half the diurnal range. These runs use Basin 1 ice conditions (Table 2; Sect. 2.5.4) with no base flow prescribed. Further details can be found in Supplement S2.1.

2.5.2 Sensitivity to uncertain parameters

We explored the sensitivity of our results to the values of seven parameters, shown in Fig. 3, with the prescribed ranges shown in Table 1. We studied the effect on the water level, the moulin radius at the equilibrium water level, the volume and water storage of the moulin, and the cross-sectional area of the subglacial channel at the end of a ten-day model run. These values reach equilibrium, with daily oscillations superimposed, after 3–5 days. We also tested the dependence of our results on the initial moulin radius, r_0 , which we varied across an order of magnitude from 0.65 to 5.0 meters.

We varied the value of a uniform deformation enhancement factor E over an order of magnitude ($E = 1$ to 9), which affects viscous flow of the ice surrounding the moulin. While the range of enhancement factors tested exceeds that likely to be observed in the field, the variation of an order of magnitude was chosen to match the range of other rheological parameters. We also tested the effect of ice temperature, independent of the enhancement factor. We used five different temperature profiles: cold ice temperatures (mean $\sim -15^\circ\text{C}$, range -23.1°C to the pressure melting point) measured in the center of Jakobshavn Isbr  (Iken et al., 1991); moderate ice temperatures (mean $\sim -7^\circ\text{C}$, range -13.5°C to the pressure melting point) measured at the GULL site in P kitsoq (L thi et al., 2015; Ryser et al., 2014); warmer ice temperatures (mean $\sim -5^\circ\text{C}$, range -9.3°C to the pressure melting point) measured at the FOXX site in P kitsoq (L thi et al., 2015; Ryser et al., 2014); a hypothetical linear profile from -5°C at the surface to 0°C at the bed; and, finally, a fully temperate ice column. These different ice temperature scenarios affected the creep closure rates of ice through the temperature-dependent softness parameter A by approximately a factor of 6 from the coldest profile (Iken et al., 1993) compared to the fully temperate column.

We also examined moulin sensitivity to elastic deformation by varying Young's modulus (E) of the ice column between 1–9 GPa (Vaughan, 1995) and the sensitivity to the values of friction factors for the moulin walls. MouSh has two friction factors: f_m (below the water line) and f_w (above the water line). We varied these friction factors across two orders of magnitude. We did not vary the subglacial channel friction factor. Finally, we varied values for basal ice softness over two

orders of magnitude and independently examined moulins over a range of ice thicknesses (670–1570 m) and corresponding distance from the terminus (~20–110 km), which in combination results in variations in hydraulic gradient.

2.5.3 Sensitivity to local conditions

We examined moulins over a range of ice thicknesses and corresponding distances from the terminus (Table 2). Each moulin is associated with a supraglacial basin derived by Yang and Smith (2016). The moulins were selected based on ice thicknesses that broadly represent the range of ice thicknesses within the ablation zone of the western Greenland Ice Sheet and supraglacial drainage basin sizes and geometries that were visually similar to nearby drainage basins and approximately representative of the mean supraglacial drainage basin area for the given ice thicknesses (553m, 741m, and 1315m). To derive broadly representative Q_{in} values for each basin, we integrate 3-hourly modeled surface melting from a downscaled version of MERRA-2 (Gelaro et al., 2017) over the surface area of each moulin surface drainage basin. We then use synthetic unit hydrograph parameters derived for a supraglacial basin from western Greenland during the middle of the 2015 melt season (Smith et al., 2017) to estimate supraglacial discharge into each moulin.

The supraglacial discharge curves for each moulin are only meant to capture the seasonal change in discharge rates and diurnal variability and occasional increases in runoff due to surface melt events during the 2019 melt season. The primary goal of this exercise is to examine season-long and daily differences in model outputs, the variation in each model component (viscous, elastic and phase change), and the relative importance of each component in driving moulin geometry change at different representative locations of the western Greenland Ice Sheet.

2.5.4 Comparison to a cylindrical moulin

Subglacial models generally use a time-invariant vertical cylinder to represent moulins. To investigate and quantify the efficacy of our time-evolving moulin shape model, we drove MouSh and a static cylinder with the same meltwater inputs. We use the time-mean radius at the water level as the radius of the static cylinder; this is 1.4 m for Basin 1 and 1.3 m for Basin 2. We compared the resulting moulin water level, moulin capacity, subglacial cross-sectional area and meltwater input difference (due to melt generated within the model itself) across these runs. We compared the moulin water level values directly (*cylindrical water level – variable water level*) and compared other metrics by percentage difference (*cylindrical – variable*) / (*variable*).

2.5.5 Sensitivity to model choices

As part of MouSh development, we made several decisions about how to represent moulin geometry, water inputs, and the associated subglacial system that can directly impact the shape and water level of a modeled moulin. These decisions include (1) representing moulin cross-sectional area as a semi-elliptical, semi-circular “egg” instead of as a circle (Sect. 2.1 and 2.3.2); (2) the inclusion of estimated surface stresses in the representation of elastic deformation (Sect. 2.2.1); (3) the use of a parabolic ice sheet profile to determine the surface slope and distance to terminus for a given ice thickness (Cuffey and Paterson, 2010);

(4) the use of prescribed base flow into the subglacial component of the model (Sect. 2.4); and (5) the use of a time-evolving subglacial channel. The first two choices pertain to the complexity of the model, with our choices being more complex; simplification may be beneficial in some circumstances. Choices 4 and 5 reflect the need for a subglacial hydrologic model and would be eliminated if MouSh was configured to function with either specific observational data or with a more comprehensive subglacial model. We also test the impact of the magnitude and diurnal variability of Q_{in} on the timescale for the moulin to reach quasi-equilibrium.

To explore the impact of our model choices for decisions 1-4, we perform a series of experimental comparisons against the seasonal run for Basin 1. This allows us to capture the effect of our choices during periods of increasing and decreasing Q_{in} . We change only the parameter of interest to isolate the effect on moulin water level and moulin capacity, the two variables that most directly affect water flow within the subglacial system.

To examine the effect of an evolving versus a fixed-radius subglacial channel, we complete a series of runs with the same ice thickness and distance from terminus as Basin 1 but use a simpler Q_{in} , the cosinusoidally varying function described in Sect. 2.4.1. Further description of these runs is included in Supplement S2.2.

3 Results

3.1 Quasi-equilibrium and dependence on Q_{in}

Under uniform supraglacial inputs, the moulin water level, radius, and water capacity reach equilibrium within 10 days (red line, Fig. S2). However, supraglacial inputs are rarely, if ever, uniform, so under constantly varying conditions, the moulin will reach a ‘quasi-equilibrium’ state. This is a mean state (geometry, water level, deformation rates) with superimposed variability on the timescale of variations in Q_{in} alone. Therefore, if the forcing is diurnal, the moulin will exhibit diurnal variability from a mean state. The quasi-equilibrium state is dependent on model characteristics and parameters (Sect. 3.2; Supplement S2.2).

The magnitude and amplitude of Q_{in} alter the moulin water level and major radius at the mean water level (a proxy for moulin geometry) in predictable ways (Fig. S2 and Fig. S3). Increasing the diurnal amplitude of Q_{in} increases the diurnal variability and mean moulin water (Fig. S2b, Fig. S4). This occurs due to the disparate timescales of ice deformation versus melting. The daily increase in Q_{in} raises the water level quickly because the subglacial channel is slow to expand by melting. Conversely, the nightly fall in Q_{in} is muted by a fast contraction of the subglacial channel. This behavior drives the daily peak in moulin water level higher above the mean than daily minimum water level falls below it (Fig. S2b). The “extra” time spent with higher water levels reduces the visco-elastic closure of the moulin while also increasing turbulent melting, resulting in a larger moulin, as indicated by the moulin radius at the mean water level (Fig. S2c). Higher diurnal amplitudes in Q_{in} magnify this effect.

As the Q_{in} magnitude increases, both the mean water level and its diurnal variability decrease (Fig. S3a-b). This occurs because the moulin becomes larger in response to increasing Q_{in} and subsequent increases in subglacial discharge. As the

31 moulin and subglacial channel widen, they can readily accommodate the fluctuations in Q_{in} with more limited variations in
32 moulin water level. This accommodation is evident in the moulin radius at the mean water level (Fig. S3c). Higher Q_{in}
33 magnitude drives a linear increase in melt rates within the moulin alongside nonlinear increases in visco-elastic deformation,
34 causing an overall nonlinear increase in mean moulin water level (Fig. S4). However, when moulin water levels exceed
35 flotation, the moulin grows due to both visco-elastic deformation and melting, resulting in a larger than expected moulin (red
36 line, Fig. S3c).

37 **3.2 Sensitivity of MouSh to parameter values and deformational processes**

38 A range of ice characteristics affect the time evolution of moulin geometry. These include the initial moulin size, temperature
39 and viscosity of the ice column, viscosity of basal ice, friction factors, and ice thickness. Some of these factors are highly
40 spatially variable (e.g., ice thickness) and others are poorly known (e.g., basal ice viscosity). We quantify the effect of these
41 factors on moulin water level and moulin volume, moulin geometry, and subglacial channel cross-sectional area over both
42 multi-day and diurnal timescales by performing multiple independent sensitivity studies (Sect. 2.3).

43 We find that moulins reach a quasi-equilibrium within 10 days, where the mean moulin water level and the moulin
44 radius at this location are constant. This quasi-equilibrium is independent of the initial moulin radius (Fig. 3a–b, Fig 4a–b),
45 apart from locations above the water line (Supplement S2.2; Fig. S2.4g) where surface deviatoric and shear stresses impact
46 moulin shape.

47 Three major parameters affect the degree of viscous and elastic deformation in the moulin: the ice flow enhancement
48 factor E , the ice temperature profile $T(z)$, and Young’s modulus E . We tested a span of reasonable values representative of
49 Greenland ice (Table 1) and found a limited effect on moulin geometry. Equilibrium moulin water level, subglacial channel
50 area, and their diurnal variabilities remain constant ($<0.1\%$ change) over the tested range of these parameters (Fig. 3d,f,h &
51 4d,f,h). Moulin capacity and water storage show moderate sensitivity ($\sim 20\%$ in equilibrium value and $\sim 40\%$ in diurnal range)
52 across the range of E and T scenarios tested; a decrease in moulin capacity and water storage pair with an increase in the diurnal
53 variability for these variables. For instance, varying E across an order of magnitude grew the equilibrium major radius by 23%
54 and shrank the equilibrium minor radius by 44%, with a net effect that moulins had 23% less volume and 20% less water
55 storage capacity in softer ice ($E = 9$) compared to harder ice ($E = 1$) (Fig. 3c–d). Similarly, the different ice temperature profiles
56 we tested caused variations of 11% in moulin major radius, 18% in moulin minor radius, and 24% in moulin capacity and
57 moulin water storage, with warmer ice hosting smaller moulins (Fig. 3e–f).

58 We varied Young’s modulus, E , across one order of magnitude. With the highest Young’s modulus, moulin major
59 radius increased by 50% compared to the lowest, minor radius decreased by 15%, moulin water volume increased by 38%,
60 and moulin capacity increased by 56% (Fig. 3g–h). The equilibrium water level decreased insignificantly ($<0.1\%$) and the
61 subglacial channel area increased insignificantly ($<0.1\%$) across this range of E . These effects are comparable to those of F^* ,
62 which we also varied over one order of magnitude, and T , which changed the englacial flow-law parameter A by approximately
63 a factor of 6.

64 In contrast to the above parameters, we find that moulin geometry is strongly sensitive to the choice of basal ice
65 softness and the friction factors used within the moulin (f_m and f_{oc}). Melting due to the dissipation of turbulent energy is partially
66 controlled by the friction factors chosen for the moulin walls. The friction factor above the water line (f_{oc} , “open channel”)
67 does not significantly affect moulin water level ($<0.1\%$ change for f_{oc} variations over two orders of magnitude), moulin volume
68 (4%), moulin water storage (2%), or subglacial channel area ($<0.1\%$) over either long or diurnal timescales (Fig. 3m–n and
69 4m–n). However, like the deformational parameters, the open channel friction factor does affect moulin radii, with the major
70 radius growing by 36% as the open channel friction factor increases over two orders of magnitude, and the minor radius
71 decreasing by 27%. This dampens the diurnal variability in both radii (Fig. 4m).

72 Increasing the friction factor below the water line (f_m) had similar effects to changing f_{oc} . Increasing f_m by two orders
73 of magnitude increased the cross-sectional area of the moulin by 106%, via a 15% increase in the major radius and a 95%
74 increase in the minor radius. The water volume increased by 116% and the storage capacity increased by 100% (Fig. 3k–l)
75 while the equilibrium water level and the subglacial channel area changed by $<0.1\%$. Increasing f_m also increased the diurnal
76 variability of the moulin capacity and water storage (Fig. 4k–l) by increasing the diurnal differential melt rate.

77 The two parameters which have the largest impact on moulin water level are the basal ice softness A and the moulin
78 location on the ice sheet, described jointly by the ice thickness (H_i) and distance from the terminus (L). This sensitivity indicates
79 an interplay among these parameters, the subglacial hydraulic gradient, and moulin water level. We varied basal ice softness
80 A by two orders of magnitude. Softer basal ice increased the size and storage capacity of the moulin: the major radius by 21%,
81 the minor radius by 25%, the total capacity by 88%, and the stored water volume by 112% (Fig. 3i–j). These changes also
82 increased the equilibrium water level by 57% and the subglacial channel area by 24%, unlike tests on englacial parameters (E ,
83 T , and Y), which did not affect the water level or subglacial channel area. These changes occur because softer basal ice increases
84 the rate of subglacial creep closure, which reduces subglacial channel cross-sectional area, which reduces water throughflow
85 in the moulin and increases water level, which in turn reduces the amount of viscous and elastic radial closure in the moulin.
86 Increasing the basal ice softness to approximately $10^{-23} \text{ Pa}^{-3}\text{s}^{-1}$ increases the diurnal variability in the sizes of the subglacial
87 channel and moulin (Fig. 4i–j); however, increasing A above this value causes moulin water levels to rise high enough that
88 diurnal fluctuations are truncated by the ice thickness resulting in an observed decrease in diurnal range that would not be
89 present in thicker ice (Fig. 4j).

90 We co-varied ice thickness and distance from terminus using a parabolic approximation for a perfectly plastic ice
91 surface profile (Cuffey and Paterson, 2010). Variations in ice thickness from 670 to 1570 m (80%) increase equilibrium
92 subglacial conditions by 20% and increase equilibrium water levels by 107% (Fig. 3o–p). Increasing ice thickness and distance
93 from the terminus increases the moulin major and minor radii by 4%, increases moulin volume by 97%, and increases moulin
94 water storage by 114% (Fig. 4p). We also find significant increases in diurnal variability in subglacial channel size (28%),
95 water level (105%), moulin radii (major radius 85% and minor radius 22%), moulin volume (130%), and moulin water storage
96 (140%) in thicker ice farther from the terminus (Fig. 4o–p).

97 Overall, we find that MouSh-modeled moulins are primarily sensitive to the friction factors for water flow through
98 the moulin, basal ice softness, and location on the ice sheet (ice thickness and distance from the terminus). The results are less
99 sensitive to englacial material factors that govern elastic and viscous deformation. The observed sensitivity to the ice thickness
00 and distance from terminus signals that moulin geometry can vary spatially. The sensitivity to friction factors and basal ice
01 softness indicates that the values of these poorly constrained parameters should be carefully chosen and kept in mind when
02 interpreting model output.

03 3.2.1 Contributions to moulin shape

04 Figure 5 illustrates the role of each process that changes moulin radius under equilibrium conditions: phase change, viscous
05 deformation, and elastic deformation. We use standard values for all parameters (Table 1) and we vary ice thickness and
06 distance from terminus. We find that moulin shape is quite similar across different ice thicknesses, while mean water level,
07 moulin capacity (Fig. 5a–e) and the diurnal range in moulin radius (Fig. 5g) increase with ice thickness. We also analyze
08 temporal variations in each process (Fig. 5g). The times of maximum melt and maximum viscous closure are slightly offset,
09 with peak melting occurring during the most rapid decline in viscous deformation (Fig. 5g). This offset aligns with the rising
10 limb of the input hydrograph, when the moulin is small and increases in Q_{in} raise water level and, in turn, elevate englacial
11 melt rates and reduce viscous deformation.

12 Melt rates both above and below the water line contribute to moulin growth (Fig. 5f–g). Melt above the water level
13 occurs due to stream or waterfall erosive processes, which in MouSh occur only within a fraction of the total circumference
14 (Fig. 2a,d), which manifests as growth of the major radius. The actual rate of melting, however, is also dictated by the area
15 over which water flow occurs, which under our parameterization is related to the cross-sectional area of the moulin at any
16 given depth (Fig. 5f).

17 Elastic deformation, like viscous deformation, closes the moulin except when the water level is above flotation. Elastic
18 deformation rates are generally smaller than viscous rates, except between ~100–300 meters above the bed, where viscous
19 deformation is minimized by cold ice temperatures (Lüthi et al., 2015; Ryser et al., 2014). Diurnally, elastic deformation varies
20 with a similar pattern to viscous deformation, though over less range.

21 3.3 Moulin shape in different environments

22 We modeled the seasonal growth and collapse of moulins in a range of environments across the Greenland Ice Sheet using
23 realistic melt forcings derived for the 2019 melt season (Sect. 2.4.1 and Sect. 2.5.3). These model runs varied with respect to
24 ice thickness, moulin distance from the terminus, base flow, and the magnitude, diurnal range, and seasonal evolution of
25 supraglacial inputs (Table 2; Fig. 6a). Overall, we find that moulin setting affects the scale of diurnal and seasonal variability
26 in the size and water capacity of moulins as well as the evolution of subglacial channels (Fig. 6 and 7).

27 The sizes of all three modeled moulins reach equilibrium with the melt forcing within 10 days of the onset of the melt
28 seasons (Fig. 6b–c). As the water flux increases over the next few weeks, each moulin grows in response to increasing

29 supraglacial inputs, both diurnally and with a long-term trend, though this growth is more significant in thicker ice (Fig. 6c
30 and Fig. 7). The subglacial channel grows with a similar pattern, but interestingly, the setting and fluxes of Basin 1 and Basin
31 2 result in very similar subglacial channel cross-sectional areas despite different water levels (Fig. 6d).

32 Though the three moulins all evolve in a similar fashion, there are differences in moulin water capacity, equilibrium
33 water level (Fig. 6), overall moulin geometry (Fig. 7), and the magnitude of englacial deformation (Fig. 8). Diurnal variation
34 in moulin capacity is slightly larger in thicker ice, due to higher rates of deformation within the moulin (Fig. 8a). This occurs
35 because daily water level fluctuations are greater in thicker ice due to the non-linearity of ice creep in conjunction with the
36 linearity of melt-driven growth (Sect. 3.1). Furthermore, in thick ice, visco-elastic deformation plays a relatively larger role in
37 moulin evolution (dark purple line in Fig. 8b), for the same reason. The only exception is during periods of low diurnal
38 variability in Q_{in} , which occurred around Day 30 of the 2019 melt season (Fig. 6a). During this period, the minimum daily
39 supraglacial inputs are quite high (Fig. 7a); moulin water levels stayed near flotation for a few days (Fig. 7b), keeping effective
40 pressure near zero and retarding deformation, and slightly increasing melt rates (Fig. 8b). In this case, viscous deformation
41 hovers around zero (though causing moulin opening), resulting in a high ratio of ecstastic to viscous deformation and a high
42 ratio of phase change to viscous deformation (purple line in Fig. 9b). There is an associated growth in moulin capacity (Fig.
43 7c). Ultimately, this is a response to multiple days where melt inputs do not exhibit substantial diurnal variability.

44 The ratio of elastic to viscous deformation generally ranges from ~ 0.4 to ~ 0.7 , depending on ice thickness (Fig. 8b).
45 Elastic deformation rates in the moulin depend on a linear function of ice thickness, while viscous rates are related to ice
46 thickness cubed. Thus, at lower elevations, the elastic contribution is maximized (~ 0.8 of viscous deformation), while at high
47 elevations, significant increases in viscous closure lowers the relative contribution of elastic deformation (~ 0.4 of viscous
48 deformation). This increase in viscous closure in thick ice also minimizes subglacial channel size in thick inland ice (Fig. 6d),
49 despite closure rates being retarded by daily periods of above overburden water pressures.

50 Each moulin has a different daily mean capacity (Fig. 7c). This, in addition to differences in supraglacial inputs,
51 ensures that daily moulin water level variations are substantially different across moulins. Basin 1 exhibits the largest variation
52 in daily moulin water level, followed by Basin 2 (Fig. 9a). Basin 3 shows the lowest daily change; however, this is due at least
53 in part to the fact that water overtops the moulin nearly daily (Fig. 6b and 7m–n). Changing water levels drive changes in
54 moulin and subglacial capacity. Over the melt season, daily change in moulin capacity can be as low as 5% during lulls in
55 diurnal melt variability (Basin 3) or as high as 31% following a recovery from a low melt day (Basin 1; Fig. 9b). However, in
56 general all moulins display a similar daily change in capacity of $\sim 20\%$.

57 The subglacial system undergoes diurnal variations in channel size between 1 and 21% (Fig. 9c). These changes are
58 similar in magnitude to daily capacity changes within the moulin but exhibit more variability across ice thicknesses and are
59 related to the daily changes in moulin water level (Fig. 9a). This suggests that the time evolution of moulin geometry dampens
60 the diurnal pressure fluctuations that drive subglacial channel growth and collapse. Evidence for this can be seen in the
61 temporal pattern of moulin water level and subglacial channel cross-sectional area (Fig. 9a,c). To test this idea, we compared
62 results from static and time-evolving moulins (Sect. 3.4).

3.4 Comparison to cylindrical moulins

To examine the role moulin evolution plays in modifying the subglacial hydrologic system, we compared moulin water levels, moulin capacity, and subglacial channel size between model runs with a fully evolving moulin and runs with a static cylindrical moulin. We performed these tests with realistic melt inputs based on the 2019 melt season (Sect. 2.4.1, 2.5.3), at moulins with low and moderate ice thicknesses (553 m – Basin 1 and 741 m – Basin 2). We defined the radius of the fixed cylinder as 1.4 m and 1.3 m for Basin 1 and 2, respectively. This results in fixed moulin cross-sectional areas ($\sim 6 \text{ m}^2$ and $\sim 5 \text{ m}^2$) that are within the range of the spatially invariant moulin cross-sectional areas $\sim 2\text{--}10 \text{ m}^2$ often prescribed in subglacial models (e.g., Andrews et al., 2014; Banwell et al., 2013; Bartholomew et al., 2012; Cowton et al., 2016; Meierbachtol et al., 2013; Werder et al., 2013). Inter-comparison of these runs allows us to examine the role moulin geometry has on subglacial pressures (Covington et al., 2020; Trunz, 2021).

Comparison of water level, moulin capacity, moulin water storage, and subglacial cross-sectional area between fixed and evolving moulins show differences on both the diurnal and seasonal times scales (Fig. 10). Moulin water levels (*fixed - variable*) can be substantial (Fig. 10a–b), with short term differences driven by variable melt conditions reaching a maximum of 97 m (Basin 1) and 145 m (Basin 2), but values can also be negative, indicating that the realistic run moulin has higher water levels, up to 46 m for Basin 1 and 25 m for Basin 2. The long-term daily average differences are -6 m and -35 m for Basin 1 and Basin 2, respectively. These differences are driven by a combination of differences in moulin capacity and subglacial channel size (Fig. 10c–f) and are despite a total increase in the meltwater input into an evolving moulin, due to melt generated from turbulent dissipation (less than 2%). These results indicate that diurnal variability is an important component not effectively represented with a cylindrical moulin.

Generally, the evolving moulin is larger (Fig. 10c–d), stores more water and maintains a larger subglacial channel (Fig. 10e,f), which all contribute to the observed difference in water levels. Midway through the melt season, the evolving moulin exhibits capacities only slightly larger than those of the fixed cylinder, but these capacity differences are exacerbated during higher Q_{in} values (Fig. 10c–d). As meltwater inputs taper at the end of the melt season (day ~ 100), the capacity and storage volume in the evolving moulin falls below that of the fixed cylinder, whose volume does not adjust in response to the forcings (Fig. 10c–d). This seasonal evolution is consistent between the two ice thicknesses tested.

The capacity differences between the variable and fixed moulin contribute directly to dampening the supraglacial input signal and dampening of moulin water levels. This, in turn, drives an increase in subglacial channel size (Fig. 10e–f), both diurnally and over the season. The seasonal difference between the variable and fixed moulin forcing is relatively constant, though punctuated by dips associated with reduced moulin water level differences (Fig. 10a–b).

3.4.5 Impact of model choices on moulin geometry

Chosen parameterizations have the potential to impact the representation of moulin water level and capacity (Supplement S2). Overall, we find that a circular geometry has limited impact on moulin water level with the circular geometry having water

95 levels that are less than 3 m higher than the egg-shaped geometry, though in nearly all instances the difference is less than
96 0.5m (Fig. S5a); however, the impact on capacity is slightly larger (the circular moulin is up to 47% smaller) and displays a
97 seasonal trend as the egg-shaped moulin elongates along its elliptical axis (Fig. S5b). Altering the deviatoric and shear stresses
98 used in the calculation of elastic deformation results in minimal changes, primarily above the water line. Moulin water levels
99 are typically within 0.25 m of the control run (Fig. S5c). Prescribing the surface stresses to be zero results in a maximum
00 increase in moulin capacity of less than 10% (Fig. S5d).

01 In contrast to the previous choices, the distance from the terminus (L) and the prescribed base flow (Q_{base}) can have a
02 substantial impact on moulin water level and capacity (Fig. S5e-h). Distance from the terminus is defined by the position of a
03 given moulin on the ice sheet, and as such is not a choice or parameter per se; and base flow is used here to mitigate the use of
04 a simplistic subglacial hydrology model. Finally, we examine the impact of fixing the subglacial channel cross-sectional area
05 S . Experimental results using a fixed S and a seasonally evolving melt curve resulted in extremely low and extremely high
06 water levels resulting in complete moulin collapse or runaway growth, respectively. Therefore, we explore the impact of fixing
07 S using a constant mean Q_{in} with an overlaid diurnal variability (Supplement Sect. S2.2.6). When the fixed S is smaller than a
08 variable S , moulin water levels are higher and exhibit less diurnal variability while moulin capacity is larger (Fig. S6). Further
09 details are included in the Supplement S2.

10 4 Discussion

11 4.1 Timescales of moulin formation and evolution

12 We consider the formation timescales of moulins in the context of the shape evolution of a mature moulin. Using MouSh, we
13 find that in the absence of external forcing, such as time-variable Q_{in} , the size of a moulin reaches its equilibrium value in ~1–
14 10 days depending on ice and supraglacial input conditions (Fig. 5g, Fig. S2 and Fig. S3). This relaxation time is comparable
15 to the Maxwell time for ice (10–100 hours), as expected for a linear visco-elastic system. Our relaxation time also compares
16 well to the equilibration timescale defined by Covington et al. (2020) for their modeled moulin – subglacial conduit system,
17 which Trunz (2021) found to be 1–20 days. The most realistically sized moulins in Trunz (2021) had relaxation times closer
18 to 1 day. Their modeled system was governed solely by melt and viscous deformation and lacked elastic deformation; this may
19 explain their modestly longer relaxation time compared to ours.

20 If the process of moulin formation occurs on a timescale shorter than the 1–10-day relaxation time, the formation
21 process likely will not influence the overall form of the englacial system at equilibrium. This time range includes hydrofracture
22 during rapid lake drainage (~2 hours) and slow lake drainage (<~6 days, e.g., Selmes et al., 2011), and likely also the
23 reactivation of existing moulins in ensuing melt seasons, which, based on the timing difference between surface melt onset
24 and ice acceleration, occurs over multiple days (Andrews et al., 2018; Hoffman et al., 2011). On the other hand, moulin
25 formation by cut-and-closure occurs over years to decades (Gulley et al., 2009), well above the MouSh relaxation time and the
26 Maxwell time for ice and are more likely to create subvertical englacial channels. The interdependence of formation and

27 evolution of these moulins gives us less confidence in applying our model to moulins with cut-and-closure origins. Those
28 moulins primarily occur in temperate near-surface ice within polythermal glaciers (Gulley et al., 2009) and have not been
29 reported on the Greenland Ice Sheet.

30 **4.2 Comparison of modeled and observed moulin geometries**

31 Field observations suggest that moulin geometry evolves a high degree of complexity. Observations include anecdotes of
32 difficulty deploying sensors to the bottom of a moulin, which suggests the presence of kinks, ledges, knickpoints, and other
33 twists (Andrews et al., 2014; Covington et al., 2020; Cowton et al., 2013). Complex geometry revealed during mapping moulins
34 above the water line further suggests that moulins are not simply vertical cylindrical shafts (Covington et al., 2020; Moreau,
35 2009).

36 The MouSh model suggests that the energy transfer from turbulent meltwater entering the moulin to the surrounding
37 ice drives highly spatially variable melt rates above the water line. We incorporated the open-channel melt module to allow a
38 large opening to emerge above the water line (Fig. 5a–e and 7). When we run MouSh without the open-channel module (Sect.
39 2.3.2), the surface expression of the moulin is much smaller than observed in remote sensing images and in some cases, the
40 moulin will pinch closed at the ice-sheet surface. The open channel module also permits the development of an egg-shaped
41 geometry, which is supported by seismic observations and a resonance model of a moulin, which suggest that the moulin
42 increased in ellipticity over time (Röösli et al., 2016).

43 The value of the open-channel friction factor and the size of the spatial footprint over which melting occurs directly
44 affects the size of the upper, air-filled chamber of the moulin, which differs from when treated as circular (Fig. S5b). MouSh
45 consistently predicts ledges at the top and bottom of a consistent diurnal range in water level. Thus, we infer that energetic
46 subaerial water flow drives formation of moulin complexity above the water line, and diurnal fluctuations around a steady
47 multi-day water level drive ledge formation through a differential in melting and visco-elastic deformation above and below
48 the water line. Energetic water flow is commonly observed at stream-fed moulins near the peak of the melt season (Pitcher
49 and Smith, 2019) or during and immediately following rapid lake drainage (Chudley et al., 2019). This suggests that complex
50 moulin geometries form during periods of relatively consistent water supply. Conversely, multi-day rises in water level, driven
51 by either the surface water supply (Q_{in}) or the basal water supply (baseflow), can erase geometric complexities such as ledges,
52 as seen in MouSh results during a melt event (Fig. 7).

53 Above the water line, explored moulins in Greenland show highly variable shapes from moulin to moulin (e.g.,
54 Covington et al., 2020). Some moulins, for example the FOXX moulin, are nearly cylindrical within the explored depth (~100
55 m), with radii comparable to what we model (~2 meters). Others, like the Phobos moulin, open some tens of meters below the
56 surface to large caverns with radii approaching 10 meters, a similar morphology to karst caves with narrow entrance shafts
57 (Covington et al., 2020). MouSh can produce large openings above the water line if we use a suitably large open channel
58 friction parameter, although we lack a narrow entrance shaft and substantial vertical variability. These differences are due to
59 the inability of model parameterizations to represent complex geometries such as scalloping, plunge pools and knickpoint

60 migration (Gulley et al., 2014; Mankoff et al., 2017). Indeed, instead of modeling processes above the water line as turbulent
61 open flow, they could, in the future, be modeled using geomorphic parameterizations to model waterfall migration, perhaps
62 resulting in the clearer development of steps and plunge pools. This would require development and inclusion of a supraglacial
63 channel model as well.

64 Below the water line, MouSh results indicate that a cylinder is a reasonable representation for newly formed moulins
65 in Greenland. However, there are two caveats. First, moulin cross-sectional area, and thus water storage capacity, can vary
66 substantially over the course of a day or season (Fig. 9) and features such as englacial crevasses and reservoirs may be present
67 (e.g., McQuillan and Karlstrom, 2021). Second, in instances where moulins are reactivated over multiple melt seasons (Chu,
68 2014; Smith et al., 2017), there may be substantial deformation, as suggested by cable breakage in boreholes (Ryser et al.,
69 2014; Wright et al., 2016).

70 Observations show a wide range of moulin volumes above the water line, and moulin volumes predicted by MouSh
71 are sensitive to the value of the open-channel friction factor. Given the flexibility of model results, we should continue to rely
72 on field exploration to measure moulin size and geometry above the water line and make efforts to constrain the parameters
73 that affect sub-seasonal growth and collapse. MouSh results below the water line are less sensitive to uncertain parameter
74 values, so direct observations of underwater geometry would be less relevant for model validation than subaerial observations.
75 Overall, results from the MouSh model demonstrate that moulin geometry evolves substantially over diurnal to seasonal
76 timescales and varies with ice conditions.

77 **4.3 Diurnal water level oscillations and moulin size**

78 Moulin geometry can directly alter the relationship between meltwater inputs and moulin water level changes – the primary
79 driver of subglacial channel evolution (Andrews et al., 2014; Cowton et al., 2013). Field measurements of moulin water levels
80 indicate diurnal oscillations of 3–12% (Covington et al., 2020), ~25% (Andrews et al., 2014), and >20% (Cowton et al., 2013)
81 of overburden pressure with mean water levels of ~70% of overburden. These diurnal fluctuations are larger than those
82 observed in boreholes, which are generally, though not always, thought to sample inefficient components of the subglacial
83 hydrologic system (Andrews et al., 2014; Meierbachtol et al., 2013; Wright et al., 2016).

84 Our model results agree well with observations of moulin water level: diurnal fluctuations of 15–25% of overburden
85 pressure, with larger oscillations in thicker ice. To explain larger-than-expected daily oscillations (~10%) in thinner ice,
86 Covington et al. (2020) incorporated moulin cross-sectional area as a free parameter into their model. Matching field
87 measurements of water level required a modeled moulin radius of ~5 m (~75 m² cross-sectional area) at ice thickness 500 m
88 and a much larger moulin (radius ~20 m and cross-sectional area ~1500 m²) at ice thickness 700 m (Covington et al., 2020).
89 For comparison, MouSh predicts average radii of ~1.3 to 1.4 m (~5 m² cross-sectional area) at these ice thicknesses using
90 parameters described in Table 2, including substantially larger meltwater inputs compared to Covington et al. (2020). The
91 drastic differences in moulin size despite similar variations in diurnal water level between our study and Covington et al.
92 (2020) cannot easily be attributed to a single factor but may be explained by our limited ability to model processes above the

93 water line, our inclusion of base flow (Fig. S5g–f), substantial differences in meltwater input (e.g., Figs S2 and S3), fluctuations
94 in moulin capacity, or that their measured water levels were not from the same moulin they mapped englacially. Nevertheless,
95 we observe substantial differences in water level between fixed and variable geometry moulins that are dependent on
96 supraglacial inputs and ice conditions (Fig. 10). Water levels are less variable and generally lower in the evolving moulins
97 compared to the fixed cylindrical moulin. Thus, to match observed moulin water level fluctuations without evolving the moulin
98 geometry, a fixed cross-sectional area substantially larger than the associated subglacial channel may be necessary, as reported
99 in Covington et al. (2020).

00 **4.3 Magnitude of viscous moulin deformation**

01 Viscous and elastic deformation drive moulin closure. The role of elastic deformation in the glacial hydrologic system is
02 discussed below (Sect. 4.4); viscous deformation is the primary mechanism of moulins, boreholes and subglacial channels
03 (e.g., Catania and Neuman, 2010; Paterson, 1977, Shreve, 1972), with viscous deformation dependent on local effective
04 pressure, ice characteristics, and the geometry of the feature of interest (Flowers, 2015). Viscous deformation within our moulin
05 varies in response to meltwater inputs (Fig. 5g and Fig. 8a) with the highest deformation rates occurring at the water line (Fig.
06 5f) because at the water line, inward cryostatic pressure is least offset by outward hydrostatic pressure (see Eq. 3).

07 During our realistic runs, viscous deformation can exceed 0.5 m d^{-1} for short periods at the highest elevation (Fig.
08 8a). These deformation rates are substantially larger than measured borehole deformation rates for the primary reasons that
09 boreholes are often at or above flotation due to high subglacial water pressures (e.g., Ryser et al., 2014) or because creep
10 measurements are recorded in much smaller boreholes in colder ice (e.g., Paterson, 1997).

11 A previous moulin modeling effort focused on understanding moulin closure rates (Catania and Neumann, 2010).
12 Their results indicate that an air-filled moulin will close within a single day at the bed. However, in this instance there is no
13 opposing hydrostatic pressure. While our modeled closure rates are similar to those calculated by Catania and Neuman (2010)
14 near the surface, the moulins modeled here always contain water even at the end of the melt season (Fig. 6b). This continued
15 retention of meltwater is in line with borehole observations that subglacial pressures tend to be highest outside the melt season
16 (Downs et al., 2018) and preclude the presence of completely air-filled moulins in areas where viscous deformation rapidly
17 shuts down the hydrologic system as supraglacial inputs fall.

18 **4.4 The role of elastic deformation in ice sheet hydrology**

19 Our model results indicate that the equilibrium moulin geometry is dictated by a balance of visco-elastic deformation and
20 turbulence-driven melting (Fig. 5 and Fig. 8). In both the sensitivity study and realistic model runs, visco-elastic deformation
21 generally closes the moulin, while melting of the surrounding ice consistently opens the moulin. The exception is when moulin
22 water levels exceed flotation, in which case all three mechanisms open the moulin. In all model runs, we find that elastic and
23 viscous deformation are of the same order of magnitude, and that the elastic mode can be between 40% and 80% of the viscous
24 deformation (Fig. 5g and Fig. 8). The importance of elastic deformation holds even in the bottom few hundred meters of the

ice column, where stress conditions are similar to those in subglacial models (Fig. 5f). However, the relative importance of viscous and elastic deformation in closing the moulin is also dependent on the values of Young's modulus and viscous enhancement factor (Fig. 5 and Fig. 8). Despite extensive study of these parameters, their values are difficult to constrain. Currently, the space of viscous and elastic parameter values could conceivably allow either elastic or viscous deformation to dominate the closure of a moulin. This underscores the importance of including both modes in the MouSh model.

Current subglacial hydrology models represent subglacial channel development (opening) by turbulent energy dissipation and destruction (closing) by viscous deformation alone. Some more recent work involving elastically responding storage elements or elastic flexure of the ice sheet has occurred (Clarke, 1996; Dow et al., 2015), and there have been efforts to use elastic deformation or fluid compressibility to improve numeric stability of channel equations (Clarke, 2003; Spring and Hutter, 1981, 1982). Interestingly, Clarke (2003) chose to use fluid compressibility due to model integration times. Yet, elastic deformation has generally been omitted from current models of subglacial channelization, even when modeling rapid changes in meltwater inputs (< 1 day; e.g., Hewitt, 2013; Hoffman et al., 2016; Werder et al., 2013). This choice is likely because the role of elastic deformation was considered negligible over timescales of subglacial evolution (e.g., days to weeks). However, the importance of elastic deformation in diurnally closing moulins, particularly in thinner ice (Fig. 8b), suggests that its exclusion from subglacial channel models could result in the underestimation of channel closure rates when water levels are below flotation.

This leads us to ask why elastic deformation is absent from subglacial models, particularly because its importance relative to viscous deformation is difficult to constrain given the current range of observed Young's modulus (Vaughan, 1995). Hypothetical subglacial channel models that included elastic deformation alongside viscous deformation would show less temporal asymmetry, particularly in thinner ice, where channel closure may be strongly dictated by elastic deformation. Elastic-incorporating models would also likely predict larger diurnal variations in channel size and moulin water level. This in turn would incite stronger local pressure gradients at the bed, increasing connectivity between the channel and the surrounding distributed system.

4.5 Moulin geometry and the englacial void ratio

Subglacial hydrology models use an englacial void ratio parameter to represent bulk storage and release of meltwater in the englacial system (see Flowers and Clarke (2002) for the best description). Because the englacial void ratio acts as short term, pressure dependent, storage for subglacial models, it can improve the representation of diurnal water pressure fluctuations in subglacial models (Flowers and Clarke, 2002) and, if coupled to a dynamical ice model, corresponding diurnal variations in ice flow. This parameter represents bulk behavior and is usually set constant over the model domain, yet it must be tuned by comparing to local observations (e.g., Bartholomaus et al., 2011; Hoffman et al., 2016; Werder et al., 2013). The inclusion of moulins, potentially in addition to time varying representation of englacial fractures (Gajek et al., 2021), that evolve in response to meltwater inputs and subglacial pressures could reduce subglacial model dependence on this highly parameterized englacial

storage, particularly in light of observations of time varying englacial features (Church et al., 2020) and meltwater content (e.g., Vankova et al, 2018).

Recent work suggests that fluctuations in water level are controlled by the size of the moulin near the water level (Trunz, 2021): moulins with larger cross-sectional areas have lower diurnal variability in water level, if given the same melt input. Furthermore, our results suggest that the amount of water stored in a moulin is highly dependent on local conditions, such as water pressure on daily to seasonal timescales, and ice thickness (Fig. 6c and Fig. 7). Thus, we explore the possibility that detailed model-based information on moulin sizes and shapes could inform the englacial void ratio used in subglacial hydrology models. This would allow time dependence and finer spatial variation, including in the vertical dimension as well as horizontal, than is currently possible with a bulk parameter. Periods of increased supraglacial inputs can require a sizable increase in englacial void ratio for subglacial models to accurately predict moulin water level (Hoffman et al., 2016). During these times, MouSh predicts rapid growth in moulin capacity (Fig. 7 and Fig. 8). This correspondence suggests plausible close ties between moulin size and the englacial void ratio: moulin size modifies englacial storage spatially and temporally.

MouSh can be used to infer both moulin size and shape, which would effectively change the englacial void ratio in all three spatial dimensions and time. The shape of the moulin imposes new temporal variability on water level and subglacial channel size: moulins with large near-surface chambers that funnel down to become narrower at the water line, for instance, have lower-magnitude and smoother variations in water level compared to cylindrical moulins, whereas moulins with small surface openings that widen toward the water line have larger and peakier water-level variations (Trunz, 2021). Thus, when the shape of a moulin is explicitly resolved, any assumed linear relationship between melt input rates and the range or pattern of oscillations in water level and subglacial channel size breaks down. The relationship also changes with the water level in the moulin; hence it varies in time.

MouSh demonstrates that moulin capacity can vary greatly both seasonally and during short periods of large variability in supraglacial input. Moulin growth rates are largest particularly when water levels are above flotation, maximizing turbulent melting and outward visco-elastic deformation. Our results show that moulin capacity changes by ~20% daily (Fig. 10) and ~50–100% over the melt season (Fig. 6c and Fig. 8b), with larger changes during periods of large supraglacial input variability and at locations with thicker ice. These variations in moulin shape and size may explain difficulties with modeling subglacial behavior during melt events (Cowton et al., 2016), which are sometimes addressed by temporarily increasing englacial storage (Hoffman et al., 2016). Our results with MouSh lead us to recommend that moulin shape and size be modeled alongside the evolution of the subglacial system, especially during periods of large meltwater variability, in order to more accurately predict subglacial water pressures and ice motion.

Practical limits on model complexity or computational costs may preclude fully time-evolving moulin geometries. While not ideal, an arbitrary static shape is still preferable to a static cylinder (Trunz, 2021). Therefore, we interpret our moulin shape results (Fig. 7) to recommend a representative shape for a static moulin. Below the water line, a cylinder is a reasonable approximation, especially in thinner ice or for newly made moulins, for which full-column ice deformation is minimized. Above the water line, moulin shape is widely variable in time, by location, and across parameter combinations. It is especially

sensitive to the friction parameter for open-channel flow (Fig. 3m and Fig. 4m), with low friction values making bottle-shaped moulins that have narrow necks above the water line and larger chambers below the water line, and high friction values making goblet-shaped moulins with open rooms and amphitheaters above the water line atop a narrower geometry below the water line. Exploration of Greenland moulins to date has uncovered multiple goblet-shaped moulins and a few instances of near-cylindrical moulins, but no bottle-shaped moulins (Covington et al., 2020; Moreau, 2009; Trunz, 2021). Overall, our MouSh results support goblet-shaped moulins, although with great variation in the height and width of the upper chamber.

4.6 Limitations of the current MouSh englacial – subglacial model

Moulins are a dynamic component of the channelized englacial–subglacial system, and explicitly modeling their evolution can therefore improve the accuracy of englacial–subglacial hydrology models (Sect. 3.4). MouSh currently uses a single subglacial channel to represent the entire subglacial system, limiting its accuracy. An optional baseflow term, which parametrizes subglacial water flow from surrounding regions, improves MouSh performance. This base flow, added directly to the subglacial channel, is necessary to produce realistic equilibrium water levels with the realistic supraglacial inputs we prescribed (Fig. 6a). The baseflow value we used does not explicitly represent any specific process because our model runs resolve only a single moulin connected to a single channel, whereas in the real world, multiple moulins feed a network of channels. The idealized baseflow term conceptually connects to multiple potential water sources, including (1) basal melting from geothermal and frictional heating, (2) supraglacial water delivered via nearby moulins that are connected to the same subglacial channel, and (3) water that moves from the channelized system to the surrounding inefficient system at high pressures and then flows back into the subglacial channel at lower water pressures (Hoffman et al., 2016; Mair et al., 2001, 2002; Tedstone et al., 2015).

The addition of baseflow maintains a larger, less variable subglacial channel. This can alternately be achieved by lessening the local hydraulic gradient, thus increasing the mean water pressure along a given reach. This may locally occur where one subglacial channel enters another in an arborescent network (Fountain and Walder, 1998). MouSh currently does not have an interconnected network of channels; however, this is under development (Trunz, 2021).

We use a highly simplified model of the subglacial hydrology system: a single channel that connects the moulin to the ice-sheet margin. Yet, MouSh results clearly indicate that including and evolving a moulin can reduce diurnal and long-term subglacial pressures via time-varying storage in the moulin (Fig. 10a). This has implications for subglacial channel growth and size (Fig. 10c). Nevertheless, MouSh currently lacks a distributed system, which limits its fidelity for assimilating daily meltwater volumes into the subglacial system. Realistically, the channelized subglacial system cannot always accommodate the full volume of meltwater produced during summer days, and a portion of this water goes into the distributed system (e.g., Mair et al., 2001, 2002). In our model, however, when the channelized system is overwhelmed, the water level in the moulin rises above what is typically observed, and sometimes even exceeds the height of the ice (Figs. 6b, S2b, S3b). The melt-driven opening and creep closure processes in the subglacial model explain this behavior: A lower water input to the moulin (Q_{in}) lowers the water flux into the subglacial system (Q_{out}), which lowers the melt rates that keep subglacial channels open, reducing the size of the subglacial channels and thus further reducing the subglacial water flux. This increases the water level in the

24 moulin. Thus, a reduced rate of surface melt can counterintuitively raise the modeled water level (Fig. 6 around day 30),
25 whereas in reality, much of that water would enter the inefficient subglacial hydrologic system when moulin water levels
26 exceed flotation. If the moulin model were coupled to a two-component subglacial model that represents the inefficient system
27 alongside the channelized system, we would anticipate a much-improved ability to assimilate a wide range of meltwater input
28 rates.

29 **5 Conclusions**

30 Results from the MouSh model show that moulins are not static cylinders. Their shapes oscillate daily by some 30% around
31 an equilibrium value reached within the first week of diurnally oscillating inputs. Daily fluctuations change the water volume
32 held in the englacial hydrologic system, which in turn influences the evolution of the subglacial channels that moulins feed.
33 When we represent a moulin as a static cylinder in our englacial–subglacial hydrology model, these daily fluctuations can be
34 substantially over estimated or underestimated, affecting the hydraulic gradient of the subglacial system. Modeled moulin size
35 and shape may provide a more realistic representation of moulin water level and the englacial void ratio commonly used in
36 subglacial hydrology models, particularly with future efforts to improve the parameterization of moulin development above
37 the water line. This could be achieved by using an englacial hydrology – channelized subglacial system model, such as the
38 MouSh model we present here, to characterize variability in moulin size and shape, or by coupling moulin models to more
39 complete models of the subglacial system (channelized, distributed, and optionally weakly connected) to make a unified
40 englacial–subglacial hydrology model system. Improving the representation of the englacial–subglacial system to explicitly
41 include moulins would have greatest efficacy during periods of rapidly varying supraglacial input (e.g., during the beginning
42 and end of the melt season and during melt events) and in inland areas with thick ice and high overburden pressures. These are
43 coincident with situations where subglacial models without moulins, or with implicitly static moulins, tend to perform poorly.

44
45 *Code and Data availability.* The Moulin Shape model is publicly available at [https://github.com/kpoinar/moulin-physical-](https://github.com/kpoinar/moulin-physical-model/tree/MouSh-beta-revisions)
46 [model/tree/MouSh-beta-revisions](https://github.com/kpoinar/moulin-physical-model/tree/MouSh-beta-revisions) (we will make a release when revisions are complete). The model results used in the analysis
47 presented here are archived at the University at Buffalo Libraries at <http://hdl.handle.net/10477/82587>.

48
49 *Author contributions.* L.C.A. and K.P. jointly conceived of and developed the MouSh model. Both L.C.A. and K.P. designed
50 the study, executed the model runs, analyzed the data, produced the figures, and wrote the manuscript. C.T. implemented the
51 subglacial module, participated in discussions, and edited the manuscript.

52
53 *Acknowledgements.* This work was supported by NASA Cryosphere grant 80NSSC19K0054 (L.C.A. and K.P.), the Global
54 Modeling and Assimilation Office at NASA Goddard Space Flight Center funded under the NASA Modeling, Analysis, and
55 Prediction (MAP) program (L.C.A.), the Research and Education in eNergy, Environment and Water (RENEW) Institute at

the University at Buffalo (K.P.), and the United States National Science Foundation award number NSF-ANS 1603835 (C.T.). We acknowledge DigitalGlobe, Inc. for providing WorldView images via the Enhanced View Web Hosting Services and the support therein provided by the Polar Geospatial Center under NSF-OPP awards 1043681 and 1559691. We thank two anonymous reviewers and editor Dr. Elizabeth Bagshaw for constructive feedback which substantially improved manuscript clarity and completeness.

Competing interests. An author is a member of the editorial board of The Cryosphere. The peer-review process was guided by an independent editor, and the authors have no other competing interests to declare.

References

- Aadnøy, B. S.: A complete elastic model for fluid-induced and in-situ generated stresses with the presence of a borehole, *Energy Sources*, 9, 239–259, 1987.
- Alley, R. B.: Flow-law hypotheses for ice-sheet modeling, *J. Glac.*, 38(129), 245–256, <https://doi.org/10.3189/S0022143000003658>, 1992.
- Alley, R. B., Dupont, T. K., Parizek, B. R., and Anandakrishnan, S.: Access of surface meltwater to beds of sub-freezing glaciers: preliminary insights, *Ann. Glac.*, 40, 8–14, <https://doi.org/10.3189/172756405781813483>, 2005.
- Amadei, B.: *Rock Anisotropy and the Theory of Stress Measurements*, Springer-Verlag, Berlin, New York., 1983.
- Andrews, L. C., Catania, G. A., Hoffman, M. J., Gulley, J. D., Lüthi, M. P., Ryser, C., Hawley, R. L. and Neumann, T. A.: Direct observations of evolving subglacial drainage beneath the Greenland Ice Sheet, *Nature*, 514(7520), 80–83, <https://doi.org/10.1038/nature13796>, 2014.
- Andrews, L. C., Hoffman, M. J., Neumann, T. A., Catania, G. A., Lüthi, M. P., Hawley, R. L., Schild, K. M., Ryser, C. and Morriss, B. F.: Seasonal Evolution of the Subglacial Hydrologic System Modified by Supraglacial Lake Drainage in Western Greenland, *J. Geophys. Res. Earth Surf.*, 123(6), 1479–1496, <https://doi.org/10.1029/2017JF004585>, 2018.
- Banwell, A. F., Willis, I. C. and Arnold, N. S.: Modeling subglacial water routing at Paakitsoq, W Greenland, *J. Geophys. Res. Earth Surf.*, 118(3), 1282–1295, <https://doi.org/10.1002/jgrf.20093>, 2013.
- Banwell, A. F., Hewitt, I., Willis, I. and Arnold, N.: Moulin density controls drainage development beneath the Greenland ice sheet, *J. Geophys. Res. Earth Surf.*, 2015JF003801, <https://doi.org/10.1002/2015JF003801>, 2016.
- Bartholomew, T. C., Anderson, R. S. and Anderson, S. P.: Growth and collapse of the distributed subglacial hydrologic system of Kennicott Glacier, Alaska, USA, and its effects on basal motion, *J. Glac.*, 57(206), 985–1002, <https://doi.org/10.3189/002214311798843269>, 2011.
- Bartholomew, I. D., Nienow, P., Sole, A., Mair, D., Cowton, T. and King, M. A.: Short-term variability in Greenland Ice Sheet motion forced by time-varying meltwater drainage: Implications for the relationship between subglacial drainage system behavior and ice velocity, *J. Geophys. Res. Earth Surf.*, 117(F3), F03002, <https://doi.org/10.1029/2011JF002220>, 2012.
- Bell, R. E.: The role of subglacial water in ice-sheet mass balance, *Nature Geosci.*, 1(5), 297–304, <https://doi.org/10.1038/ngeo186>, 2008.

90 Benn, D. I., Thompson, S., Gulley, J., Mertes, J., Luckman, A. and Nicholson, L.: Structure and evolution of the drainage
 91 system of a Himalayan debris-covered glacier, and its relationship with patterns of mass loss, *TC*, 11, 2247–2264,
 92 <https://doi.org/10.5194/tc-11-2247-2017>, 2017.

93 Boulton, G. S., Lunn, R., Vidstrand, P. and Zatsepin, S.: Subglacial drainage by groundwater–channel coupling, and the origin
 94 of esker systems: part II—theory and simulation of a modern system, *Quat. Sci. Rev.*, 26(7–8), 1091–1105,
 95 <https://doi.org/10.1016/j.quascirev.2007.01.006>, 2007.

96 Catania, G. A. and Neumann, T. A.: Persistent englacial drainage features in the Greenland Ice Sheet, *Geophys. Res. Lett.*,
 97 37(2), L02501, <https://doi.org/10.1029/2009GL041108>, 2010.

98 Catania, G. A., Neumann, T. A. and Price, S. F.: Characterizing englacial drainage in the ablation zone of the Greenland Ice
 99 Sheet, *J. Glac.*, 54(187), 567–578, <https://doi.org/10.3189/002214308786570854>, 2008.

00 Chandler, D. M., Wadham, J. L., Lis, G. P., Cowton, T., Sole, A., Bartholomew, I., Telling, J., Nienow, P., Bagshaw, E. B.,
 01 Mair, D., Vinen, S. and Hubbard, A.: Evolution of the subglacial drainage system beneath the Greenland Ice Sheet revealed
 02 by tracers, *Nature Geosci*, 6(3), 195–198, <https://doi.org/10.1038/ngeo1737>, 2013.

03 Chu, V. W.: Greenland Ice Sheet hydrology: A review, *Prog. Phys. Geogr.*, 38(1), 19–54,
 04 <https://doi.org/10.1177/0309133313507075>, 2014.

05 Chudley, T. R., Christoffersen, P., Doyle, S. H., Bougamont, M., Schoonman, C. M., Hubbard, B. and James, M. R.:
 06 Supraglacial lake drainage at a fast-flowing Greenlandic outlet glacier, *PNAS*, 116(51), 25468–25477,
 07 <https://doi.org/10.1073/pnas.1913685116>, 2019.

08 Church, G., Grab, M., Schmelzbach, C., Bauder, A., and Maurer, H.: Monitoring the seasonal changes of an englacial conduit
 09 network using repeated ground-penetrating radar measurements, *TC*, 14, 3269–3286, <https://doi.org/10.5194/tc-14-3269-2020>,
 10 2020.

11 Clarke, G. K. C.: Lumped-element analysis of subglacial hydraulic circuits, *J. Geophys. Res.*, 101(B8), 17547–17559,
 12 <https://doi.org/10.1029/96JB01508>, 1996.

13 Clarke, G. K. C.: Hydraulics of subglacial outburst floods: new insights from the Spring–Hutter formulation, *J. Glac.*, 49(165),
 14 299–313, <https://doi.org/10.3189/172756503781830728>, 2003.

15 Colgan, W. and Steffen, K.: Modelling the spatial distribution of moulins near Jakobshavn, Greenland, *IOP Conf. Ser.: Earth
 16 Environ. Sci.*, 6(1), 012022, <https://doi.org/10.1088/1755-1307/6/1/012022>, 2009.

17 Colgan, W., Rajaram, H., Anderson, R., Steffen, K., Phillips, T., Joughin, I., Zwally, H. J. and Abdalati, W.: The annual
 18 glaciohydrology cycle in the ablation zone of the Greenland ice sheet: Part 1. Hydrology model, *J. Glac.*, 57(204), 697–709,
 19 <https://doi.org/10.3189/002214311797409668>, 2011.

20 Covington, M. D., Banwell, A. F., Gulley, J., Saar, M. O., Willis, I. and Wicks, C. M.: Quantifying the effects of glacier
 21 conduit geometry and recharge on proglacial hydrograph form, *J. Hydro.*, 414–415, 59–71,
 22 <https://doi.org/10.1016/j.jhydrol.2011.10.027>, 2012.

23 Covington, M. D., Gulley, J. D., Trunz, C., Mejia, J. and Gadd, W.: Moulin Volumes Regulate Subglacial Water Pressure on
 24 the Greenland Ice Sheet, *Geophys. Res. Lett.*, 47(20), e2020GL088901, <https://doi.org/10.1029/2020GL088901>, 2020.

25 Cowton, T., Nienow, P., Sole, A., Wadham, J., Lis, G., Bartholomew, I., Mair, D. and Chandler, D.: Evolution of drainage
 26 system morphology at a land-terminating Greenlandic outlet glacier, *J. Geophys. Res. Earth Surf.*, 118(1), 29–41,
 27 <https://doi.org/10.1029/2012JF002540>, 2013.

28 Cowton, T., Nienow, P., Bartholomew, I. and Mair, D.: Variability in ice motion at a land-terminating Greenlandic outlet
 29 glacier: the role of channelized and distributed drainage systems, *J. Glac.*, 62(233), 451–466,
 30 <https://doi.org/10.1017/jog.2016.36>, 2016.

31 Cuffey, K. M. and Paterson, W. S. B.: *The Physics of Glaciers*, Elsevier., 2010.

32 Das, S. B., Joughin, I., Behn, M. D., Howat, I. M., King, M. A., Lizarralde, D. and Bhatia, M. P.: Fracture Propagation to the
 33 base of the Greenland Ice Sheet during supraglacial lake drainage, *Science*, 320(5877), 778–781,
 34 <https://doi.org/10.1126/science.1153360>, 2008.

35 Dow, C. F., Kulesa, B., Rutt, I. C., Tsai, V. C., Pimentel, S., Doyle, S. H., van As, D., Lindbäck, K., Pettersson, R., Jones, G.
 36 A. and Hubbard, A.: Modeling of subglacial hydrological development following rapid supraglacial lake drainage, *J. Geophys.*
 37 *Res. Earth Surf.*, 120(6), 2014JF003333, <https://doi.org/10.1002/2014JF003333>, 2015.

38 Downs, J. Z., Johnson, J. V., Harper, J. T., Meierbachtol, T., and Werder, M. A.: Dynamic hydraulic conductivity reconciles
 39 mismatch between modeled and observed winter subglacial water pressure, *J. Geophys. Res. Earth Surf.*, 123(4), 818–836,
 40 <https://doi.org/10.1002/2017JF004522>, 2018.

41 Flowers, G. E.: Subglacial modulation of the hydrograph from glacierized basins, *Hydrol. Process.*, 22(19), 3903–3918,
 42 <https://doi.org/10.1002/hyp.7095>, 2008.

43

44 Flowers, G. E.: Modelling water flow under glaciers and ice sheets, *Proc. Math. Phys.* 471, 20140907–20140907,
 45 <https://doi.org/10.1098/rspa.2014.0907>, 2015.

46 Flowers, G. E.: Hydrology and the future of the Greenland Ice Sheet, *Nature Comm.*, 9(1), 2729,
 47 <https://doi.org/10.1038/s41467-018-05002-0>, 2018.

48 Flowers, G. E. and Clarke, G. K. C.: A multicomponent coupled model of glacier hydrology 1. Theory and synthetic examples,
 49 *J. Geophys. Res.*, 107(B11), 2287, <https://doi.org/10.1029/2001JB001122>, 2002.

50 Forster, R. R., Box, J. E., van den Broeke, M. R., Miège, C., Burgess, E. W., van Angelen, J. H., Lenaerts, J. T. M., Koenig,
 51 L. S., Paden, J., Lewis, C., Gogineni, S. P., Leuschen, C. and McConnell, J. R.: Extensive liquid meltwater storage in firn
 52 within the Greenland ice sheet, *Nature Geosci.*, 7(2), 95–98, <https://doi.org/10.1038/ngeo2043>, 2014.

53 Fountain, A. G. and Walder, J. S.: Water flow through temperate glaciers, *Rev. Geophys.*, 36(3), 299–328,
 54 <https://doi.org/10.1029/97RG03579>, 1998.

55 Gajek, W., Gräff, D., Hellmann, S., Rempel, A. W., and Walter, F.: Diurnal expansion and contraction of englacial fracture
 56 networks revealed by seismic shear wave splitting, *Comm. Earth. Environ.*, 2, 1–8, [https://doi.org/10.1038/s43247-021-00279-](https://doi.org/10.1038/s43247-021-00279-4)
 57 4, 2021.

58 Gelaro, R., McCarty, W., Suárez, M. J., Todling, R., Molod, A., Takacs, L., Randles, C. A., Darmenov, A., Bosilovich, M. G.,
 59 Reichle, R., Wargan, K., Coy, L., Cullather, R., Draper, C., Akella, S., Buchard, V., Conaty, A., da Silva, A. M., Gu, W., Kim,
 60 G.-K., Koster, R., Lucchesi, R., Merkova, D., Nielsen, J. E., Partyka, G., Pawson, S., Putman, W., Rienecker, M., Schubert, S.
 61 D., Sienkiewicz, M., and Zhao, B.: The Modern-Era Retrospective Analysis for Research and Applications, Version 2
 62 (MERRA-2), *J. Climate*, 30, 5419–5454, <https://doi.org/10.1175/JCLI-D-16-0758.1>, 2017.

63 Germain, S. L. S. and Moorman, B. J.: Long-term observations of supraglacial streams on an Arctic glacier, *J. Glac.*, 65(254),
 64 900–911, <https://doi.org/10.1017/jog.2019.60>, 2019.

- 65 Goodman, R. E.: Introduction to Rock Mechanics, 2nd ed., Wiley, New York., 1989.
- 66 Gulley, J. D., Benn, D. I., Sreaton, E. and Martin, J.: Mechanisms of englacial conduit formation and their implications for
67 subglacial recharge, *Quat. Sci. Rev.*, 28(19–20), 1984–1999, <https://doi.org/10.1016/j.quascirev.2009.04.002>, 2009.
- 68 Gulley, J. D., Spellman, P. D., Covington, M. D., Martin, J. B., Benn, D. I. and Catania, G.: Large values of hydraulic roughness
69 in subglacial conduits during conduit enlargement: implications for modeling conduit evolution, *Earth Surf. Process.
70 Landforms*, 39(3), 296–310, <https://doi.org/10.1002/esp.3447>, 2014.
- 71 Hewitt, I. J.: Seasonal changes in ice sheet motion due to melt water lubrication, *EPSL*, 371–372, 16–25,
72 <https://doi.org/10.1016/j.epsl.2013.04.022>, 2013.
- 73 Hoffman, M. J. and Price, S.: Feedbacks between coupled subglacial hydrology and glacier dynamics, *J. Geophys. Res. Earth
74 Surf.*, 119(3), 414–436, <https://doi.org/10.1002/2013JF002943>, 2014.
- 75 Hoffman, M. J., Catania, G. A., Neumann, T. A., Andrews, L. C. and Rumrill, J. A.: Links between acceleration, melting, and
76 supraglacial lake drainage of the western Greenland Ice Sheet, *J. Geophys. Res. Earth Surf.*, 116(F4), F04035,
77 <https://doi.org/10.1029/2010JF001934>, 2011.
- 78 Hoffman, M. J., Andrews, L. C., Price, S. A., Catania, G. A., Neumann, T. A., Lüthi, M. P., Gulley, J., Ryser, C., Hawley, R.
79 L. and Morris, B.: Greenland subglacial drainage evolution regulated by weakly connected regions of the bed, *Nature Comm.*,
80 7, 13903, <https://doi.org/10.1038/ncomms13903>, 2016.
- 81 Holmlund, P.: Internal geometry and evolution of moulins, *J. Glac.*, 34(117), 242–248, 1988.
- 82 Iken, A.: Measurements of water pressure in moulins as part of a movement study of the White Glacier, Axel Heiberg Island,
83 Northwest Territories, Canada, *J. Glac.*, 11(61), 53–58, 1972.
- 84 Iken, A. and Bindenschadler, R.: Combined measurements of subglacial water pressure and surface velocity of Findelengletscher,
85 Switzerland: conclusions about drainage system and sliding mechanism, *J. Glac.*, 32(110), 101–119,
86 <https://doi.org/10.3189/S002214300006936>, 1986.
- 87 Iken, A., Echelmeyer, K., Harrison, W. and Funk, M.: Mechanisms of fast flow in Jakobshavns Isbræ, West Greenland: Part
88 I. Measurements of temperature and water level in deep boreholes, *J. Glac.*, 39(131), 15–25,
89 <https://doi.org/10.1017/S0022143000015689>, 1993.
- 90 Jarosch, A. H. and Gudmundsson, M. T.: A numerical model for meltwater channel evolution in glaciers, *TC*, 6(2), 493–503,
91 <https://doi.org/10.5194/tc-6-493-2012>, 2012.
- 92 Kirsch, G.: Die Theorie der Elastizität und die Bedürfnisse der Festigkeitslehre, Springer, Berlin., 1898.
- 93 Krawczynski, M. J., Behn, M. D., Das, S. B., and Joughin, I.: Constraints on the lake volume required for hydro-fracture
94 through ice sheets, *Geophys. Res. Lett.*, 36, L10501, <https://doi.org/10.1029/2008GL036765>, 2009.
- 95 Lüthi, M. P., Ryser, C., Andrews, L. C., Catania, G. A., Funk, M., Hawley, R. L., Hoffman, M. J. and Neumann, T. A.: Heat
96 sources within the Greenland Ice Sheet: dissipation, temperate paleo-firn and cryo-hydrologic warming, *TC*, 9(1), 245–253,
97 <https://doi.org/10.5194/tc-9-245-2015>, 2015.
- 98 MacFerrin, M., Machguth, H., As, D. van, Charalampidis, C., Stevens, C. M., Heilig, A., Vandecrux, B., Langen, P. L.,
99 Mottram, R., Fettweis, X., Broeke, M. R. van den, Pfeffer, W. T., Moussavi, M. S. and Abdalati, W.: Rapid expansion of
00 Greenland’s low-permeability ice slabs, *Nature*, 573(7774), 403–407, <https://doi.org/10.1038/s41586-019-1550-3>, 2019.

01 MacGregor, J. A., Fahnestock, M. A., Colgan, W. T., Larsen, N. K., Kjeldsen, K. K. and Welker, J. M.: The age of surface-
 02 exposed ice along the northern margin of the Greenland Ice Sheet, *J. Glac.*, 66(258), 667–684,
 03 <https://doi.org/10.1017/jog.2020.62>, 2020.

04 Mair, D., Nienow, P., Willis, I. and Sharp, M.: Spatial patterns of glacier motion during a high-velocity event: Haut Glacier
 05 d’Arolla, Switzerland, *J. Glac.*, 47(156), 9–20, <https://doi.org/10.3189/172756501781832412>, 2001.

06 Mair, D., Nienow, P. W., Sharp, M. J., Wohlleben, T. and Willis, I.: Influence of subglacial drainage system evolution on
 07 glacier surface motion: Haut Glacier d’Arolla, Switzerland, *J. of Geophys Res. Solid Earth*, 107(B8),
 08 <https://doi.org/10.1029/2001JB000514>, 2002.

09 Mankoff, K. D., Gulley, J. D., Tulaczyk, S. M., Covington, M. D., Liu, X., Chen, Y., Benn, D. I. and Głowacki, P. S.:
 10 Roughness of a subglacial conduit under Hansbreen, Svalbard, *J. Glac.*, 1–13, <https://doi.org/10.1017/jog.2016.134>, 2017.

11 McGrath, D., Colgan, W., Steffen, K., Lauffenburger, P. and Balog, J.: Assessing the summer water budget of a moulin basin
 12 in the Sermeq Avannarleq ablation region, Greenland ice sheet, *J. Glac.*, 57(205), 954–964,
 13 <https://doi.org/10.3189/002214311798043735>, 2011.

14 McQuillan, M. and Karlstrom, L.: Fluid resonance in elastic-walled englacial transport networks, *J. Glac.*, 1–14,
 15 <https://doi.org/10.1017/jog.2021.48>, 2021.

16 Meierbachtol, T. W., Harper, J. and Humphrey, N.: Basal Drainage System Response to Increasing Surface Melt on the
 17 Greenland Ice Sheet, *Science*, 341(6147), 777–779, <https://doi.org/10.1126/science.1235905>, 2013.

18 Mejia, J. Z., Gulley, J. D., Trunz, C., Covington, M. D., Bartholomaus, T. C., Xie, S., and Dixon, T. H.: Isolated Cavities
 19 Dominate Greenland Ice Sheet Dynamic Response to Lake Drainage, *Geophys. Res. Lett.*, 48, e2021GL094762,
 20 <https://doi.org/10.1029/2021GL094762>, 2021.

21 Miège, C., Forster, R. R., Brucker, L., Koenig, L. S., Solomon, D. K., Paden, J. D., Box, J. E., Burgess, E. W., Miller, J. Z.,
 22 McNerney, L., Brautigam, N., Fausto, R. S. and Gogineni, S.: Spatial extent and temporal variability of Greenland firn aquifers
 23 detected by ground and airborne radars, *J. Geophys. Res. Earth Surf.*, 121(12), 2016JF003869,
 24 <https://doi.org/10.1002/2016JF003869>, 2016.

25

26 Moon, T., Joughin, I., Smith, B., van den Broeke, M. R., van de Berg, W. J., Noël, B. and Usher, M.: Distinct patterns of
 27 seasonal Greenland glacier velocity, *Geophys. Res. Lett.*, 41(20), 2014GL061836, <https://doi.org/10.1002/2014GL061836>,
 28 2014.

29 Moreau, L.: L’exploration du cryokarst glaciaire et son intérêt scientifique pour l’étude du drainage des eaux de fonte : porches,
 30 cavités, crevasses, bédrières et moulins., *Collection EDYTEM. Cahiers de géographie*, 8, 163–170, 2009.

31 Müller, F. and Iken, A.: Velocity fluctuations and water regime of Arctic valley glaciers, *IAHS*, 95, 165–182, 1973.

32 Naruse, R., Okuhira, F., Ohmae, H., Kawada, K. and Nakawo, M.: Closure Rate of a 700 m Deep Bore Hole at Mizuho Station,
 33 East Antarctica, *Ann. Glac.*, 11, 100–103, <https://doi.org/10.3189/S0260305500006406>, 1988.

34 Nossokoff, A.: Using Small Scale Physical Experiments to Improve Enthalpy Based Models of Ice Sheets, M.S., University
 35 of Colorado, Boulder, 2013.

36 Paterson, W. S. B.: Secondary and tertiary creep of glacier ice as measured by borehole closure rates, *Rev. Geophys.*, 15(1),
 37 47–55, <https://doi.org/10.1029/RG015i001p00047>, 1977.

38 Pitcher, L. H. and Smith, L. C.: Supraglacial Streams and Rivers, *Ann. Rev. Earth Planetary Sci.*, 47(1), 421–452,
39 <https://doi.org/10.1146/annurev-earth-053018-060212>, 2019.

40 Poinar, K. and Andrews, L. C.: Challenges in predicting Greenland supraglacial lake drainages at the regional scale, *TC*, 15,
41 1455–1483, <https://doi.org/10.5194/tc-15-1455-2021>, 2021.

42 Poinar, K., Joughin, I., Das, S. B., Behn, M. D., Lenaerts, J. T. M. and van den Broeke, M. R.: Limits to future expansion of
43 surface-melt-enhanced ice flow into the interior of western Greenland, *Geophys. Res. Lett.*, 42(6), 2015GL063192,
44 <https://doi.org/10.1002/2015GL063192>, 2015.

45 Poinar, K., Joughin, I., Lenaerts, J. T. M. and Broeke, M. R. V. D.: Englacial latent-heat transfer has limited influence on
46 seaward ice flux in western Greenland, *J. Glac.*, 1–16, <https://doi.org/10.1017/jog.2016.103>, 2016.

47 Poinar, K., Joughin, I., Lilien, D., Brucker, L., Kehrl, L. and Nowicki, S.: Drainage of Southeast Greenland Firn Aquifer Water
48 through Crevasses to the Bed, *Front. Earth Sci.*, 5, <https://doi.org/10.3389/feart.2017.00005>, 2017.

49 Priest, S. D.: *Discontinuity Analysis for Rock Engineering*, 1st ed., Chapman & Hall, London; New York., 1993.

50 Rösli, C., Walter, F., Ampuero, J.-P., and Kissling, E.: Seismic moulin tremor, *J. Geophys. Res. Solid Earth* 121, 5838–5858,
51 <https://doi.org/10.1002/2015JB012786>, 2016.

52 Ryser, C., Lüthi, M. P., Andrews, L. C., Hoffman, M. J., Catania, G. A., Hawley, R. L., Neumann, T. A. and Kristensen, S. S.:
53 Sustained high basal motion of the Greenland ice sheet revealed by borehole deformation, *J. Glac.*, 60(222), 647–660,
54 <https://doi.org/10.3189/2014JoG13J196>, 2014.

55 Scheingross, J. S. and Lamb, M. P.: A Mechanistic Model of Waterfall Plunge Pool Erosion into Bedrock, *J. Geophys. Res.*
56 *Earth Surf.*, 122(11), 2079–2104, <https://doi.org/10.1002/2017JF004195>, 2017.

57 Schoof, C.: Ice-sheet acceleration driven by melt supply variability, *Nature*, 468(7325), 803–806,
58 <https://doi.org/10.1038/nature09618>, 2010.

59 Selmes, N., Murray, T. and James, T. D.: Fast draining lakes on the Greenland Ice Sheet, *Geophys. Res. Lett.*, 38(15), L15501,
60 <https://doi.org/10.1029/2011GL047872>, 2011.

61 Shreve, R. L.: Movement of water in glaciers, *J. Glac.*, 11(62), 205–214, <https://doi.org/10.1017/S002214300002219X>, 1972.

62 Smith, L. C., Chu, V. W., Yang, K., Gleason, C. J., Pitcher, L. H., Rennermalm, A. K., Legleiter, C. J., Behar, A. E., Overstreet,
63 B. T., Moustafa, S. E., Tedesco, M., Forster, R. R., LeWinter, A. L., Finnegan, D. C., Sheng, Y. and Balog, J.: Efficient
64 meltwater drainage through supraglacial streams and rivers on the southwest Greenland ice sheet, *PNAS*, 112(4), 1001–1006,
65 <https://doi.org/10.1073/pnas.1413024112>, 2015.

66 Smith, L. C., Yang, K., Pitcher, L. H., Overstreet, B. T., Chu, V. W., Rennermalm, Å. K., Ryan, J. C., Cooper, M. G., Gleason,
67 C. J., Tedesco, M., Jeyaratnam, J., As, D. van, Broeke, M. R. van den, Berg, W. J. van de, Noël, B., Langen, P. L., Cullather,
68 R. I., Zhao, B., Willis, M. J., Hubbard, A., Box, J. E., Jenner, B. A. and Behar, A. E.: Direct measurements of meltwater runoff
69 on the Greenland ice sheet surface, *PNAS*, 114(50), E10622–E10631, <https://doi.org/10.1073/pnas.1707743114>, 2017.

70 Spring, U. and Hutter, K.: Numerical studies of Jökulhlaups, *Cold Reg Sci Technol.*, 4(3), 227–244,
71 [https://doi.org/10.1016/0165-232X\(81\)90006-9](https://doi.org/10.1016/0165-232X(81)90006-9), 1981.

72 Spring, U. and Hutter, K.: Conduit flow of a fluid through its solid phase and its application to intraglacial channel flow, *Int.*
73 *J. Eng. Sci.*, 20(2), 327–363, [https://doi.org/10.1016/0020-7225\(82\)90029-5](https://doi.org/10.1016/0020-7225(82)90029-5), 1982.

74 Tedstone, A. J., Nienow, P. W., Gourmelen, N., Dehecq, A., Goldberg, D. and Hanna, E.: Decadal slowdown of a land-
75 terminating sector of the Greenland Ice Sheet despite warming, *Nature*, 526(7575), 692–695,
76 <https://doi.org/10.1038/nature15722>, 2015.

77 Trunz, C.: Modeling and Measuring Water Level Fluctuations in the Greenland Ice Sheet: How Moulin Life Cycle and Shape
78 can Inform us on the Subglacial Drainage System, Ph.D., University of Arkansas, Fayetteville, Arkansas, 156 pp., 2021.

79 Turcotte, D. L. and Schubert, G.: *Geodynamics*, Cambridge University Press., 2002.

80 Vaňková, I., Voytenko, D., Nicholls, K. W., Xie, S., Parizek, B. R., and Holland, D. M.: Vertical Structure of Diurnal Englacial
81 Hydrology Cycle at Helheim Glacier, East Greenland, *Geophys. Res. Lett.*, 45, 8352–8362,
82 <https://doi.org/10.1029/2018GL077869>, 2018.

83 Vaughan, D. G.: Tidal flexure at ice shelf margins, *J. Geophys. Res. Solid Earth*, 100(B4), 6213–6224,
84 <https://doi.org/10.1029/94JB02467>, 1995.

85 Weertman, J.: Theory of water-filled crevasses in glaciers applied to vertical magma transport beneath oceanic ridges, *J.*
86 *Geophys. Res.*, 76, 1171–1183, <https://doi.org/10.1029/JB076i005p01171>, 1971.

87 Weertman, J.: Can a water-filled crevasse reach the bottom surface of a glacier?, *IASH*, 95, 139–145, 1973.

88 Weertman, J.: *Dislocation Based Fracture Mechanics*, World Scientific Publishing Company, Singapore, 1996.

89 Werder, M. A.: The hydrology of subglacial overdeepenings: A new supercooling threshold formula, *Geophys. Res. Lett.*, 43,
90 2015GL067542, <https://doi.org/10.1002/2015GL067542>, 2016.

91 Werder, M. A., Schuler, T. V. and Funk, M.: Short term variations of tracer transit speed on alpine glaciers, *TC*, 4(3), 381–
92 396, 2010.

93 Werder, M. A., Hewitt, I. J., Schoof, C. G. and Flowers, G. E.: Modeling channelized and distributed subglacial drainage in
94 two dimensions, *J. Geophys. Res. Earth Surf.*, 118(4), 2140–2158, <https://doi.org/10.1002/jgrf.20146>, 2013.

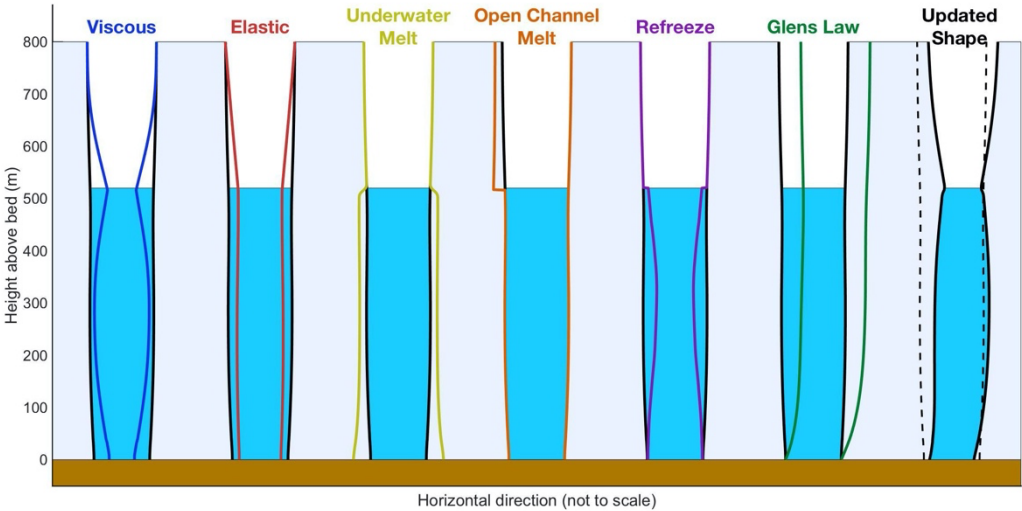
95 Williams, J. J., Gourmelen, N. and Nienow, P.: Dynamic response of the Greenland ice sheet to recent cooling, *Sci. Rep.*,
96 10(1), 1647, <https://doi.org/10.1038/s41598-020-58355-2>, 2020.

97 Wright, P. J., Harper, J. T., Humphrey, N. F. and Meierbachtol, T. W.: Measured basal water pressure variability of the western
98 Greenland Ice Sheet: Implications for hydraulic potential, *J. Geophys. Res. Earth Surf.*, 121(6), 2016JF003819,
99 <https://doi.org/10.1002/2016JF003819>, 2016.

00 Yang, K. and Smith, L. C.: Internally drained catchments dominate supraglacial hydrology of the southwest Greenland Ice
01 Sheet, *J. Geophys. Res. Earth Surf.*, 2016JF003927, <https://doi.org/10.1002/2016JF003927>, 2016.

02 Yang, K., Smith, L. C., Chu, V. W., Pitcher, L. H., Gleason, C. J., Rennermalm, A. K. and Li, M.: Fluvial morphometry of
03 supraglacial river networks on the southwest Greenland Ice Sheet, *GISci. Remote Sens.*, 53(4),
04 <https://doi.org/10.1080/15481603.2016.1162345>, 2016.

05
06
07



09

10 **Figure 1. Processes included in the MouSh model.** Black lines show a base moulin geometry that each process acts on, and colored lines

11 show the change in moulin geometry (not to scale) due to that process alone. From left to right: changes in moulin geometry due to viscous

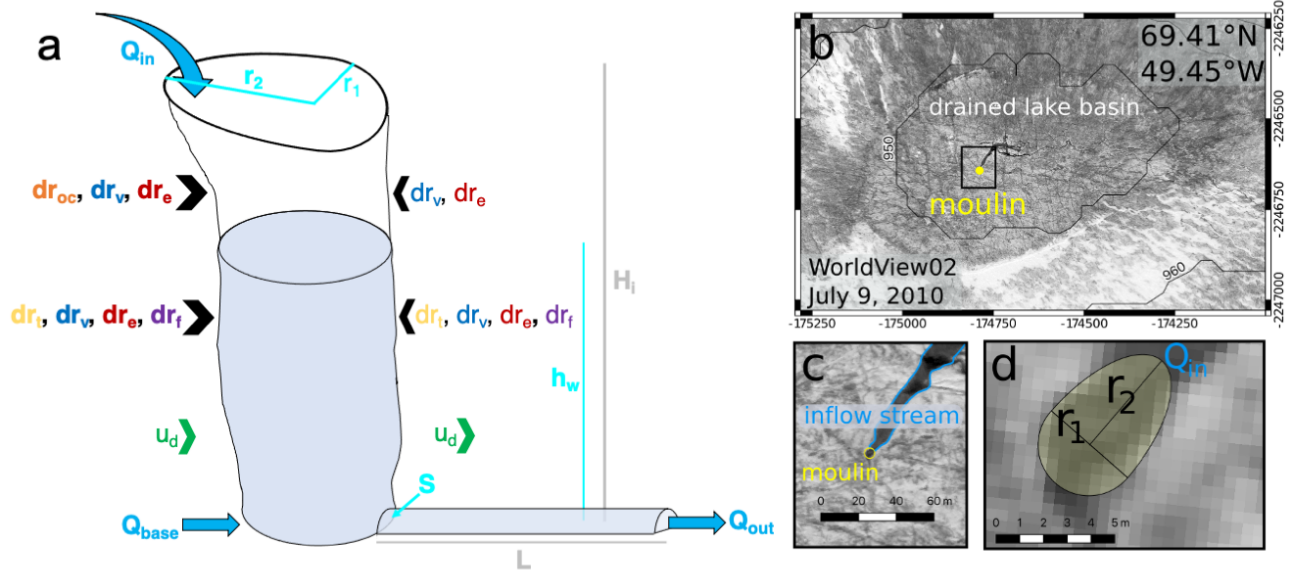
12 deformation; elastic deformation; melting by turbulent energy dissipation of flowing water inside the moulin; melting by open-channel water

13 flow along bare ice; refreezing over winter inside the moulin; and deformation due to ice motion prescribed by Glen’s flow law. Unlike the

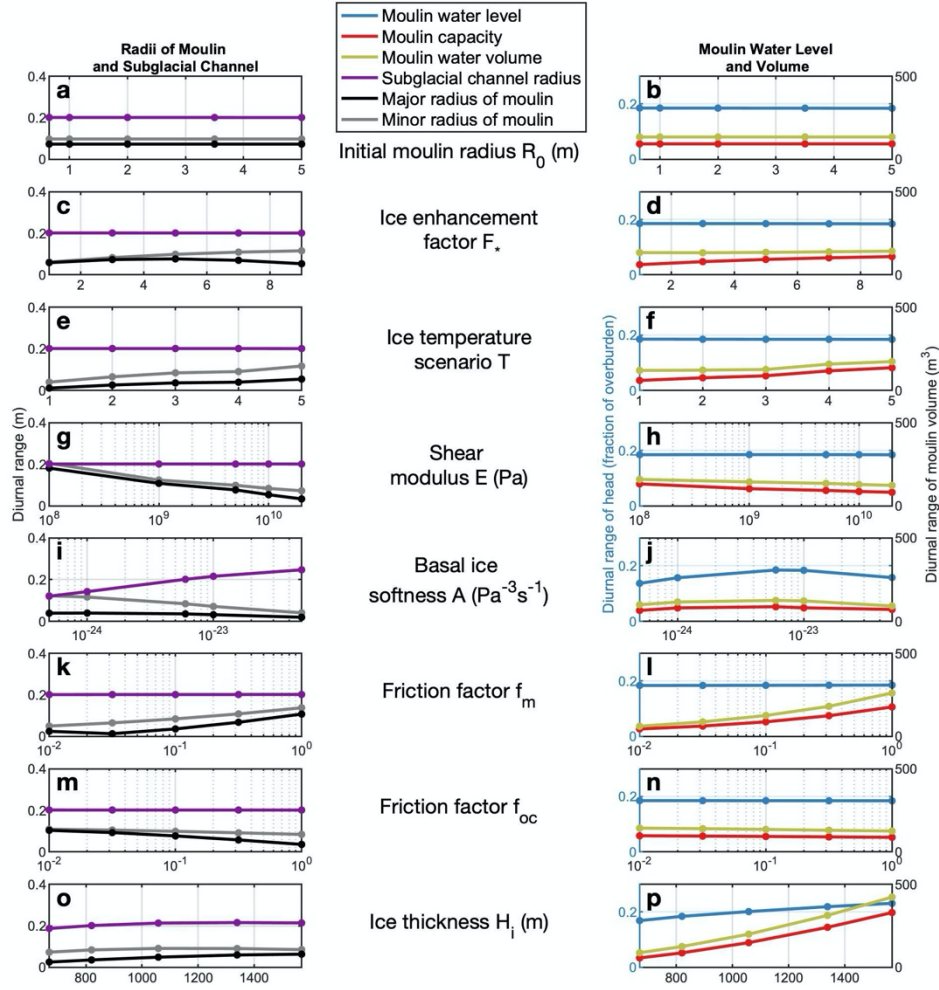
14 other components, elastic deformation is instantaneous, but applied over the model timestep (Sect. 2.2.1; Supplement S2). The right-most

15 moulin shows the moulin geometry before (dashed black lines) and after (solid black lines and blue water) a hypothetical model timestep,

16 i.e., the sum of all processes shown in the preceding panels. Changes are not to scale.



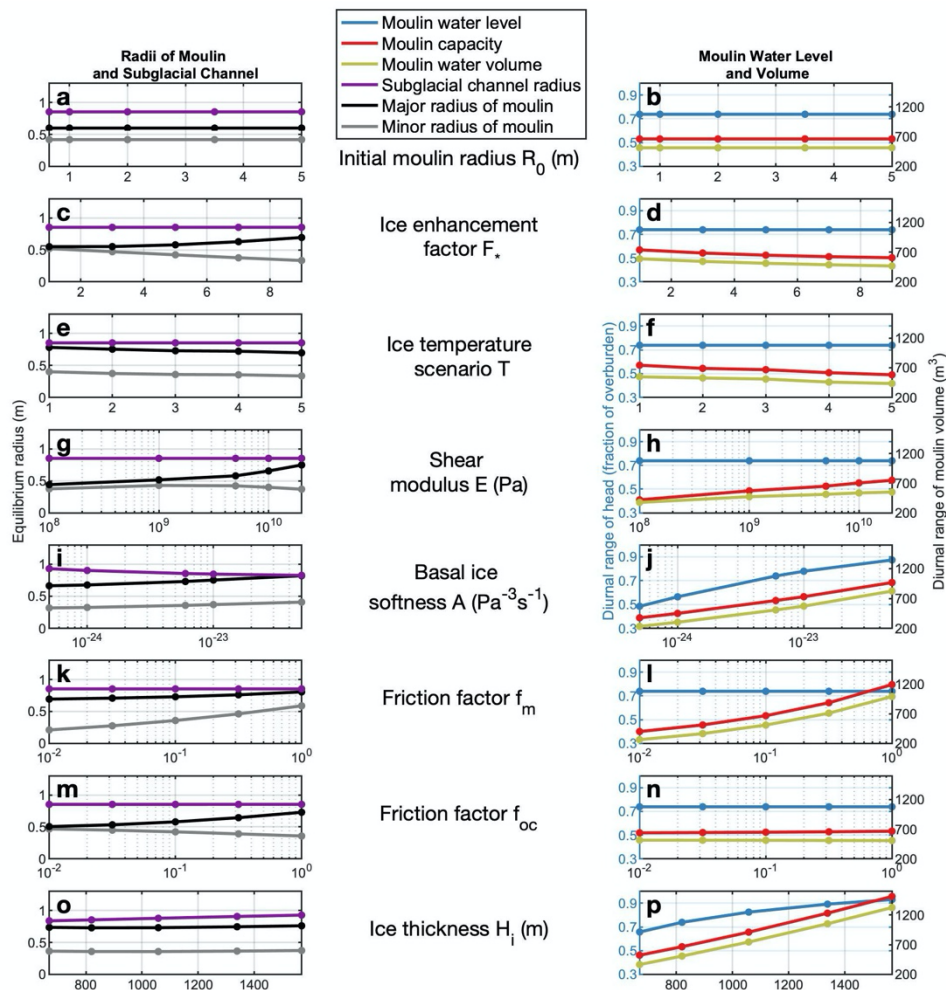
18
19 **Figure 2. MouSh geometry and surface expression of a moulin and its reflection in the MouSh model.** (a) Schematic of MouSh
20 geometry and inputs. Inflow and outflow of the system are indicated by Q_{in} , Q_{out} , and Q_{base} . Time evolving moulin and subglacial parameters
21 include moulin radii (r_1 , r_2), moulin water level (h_w), and subglacial cross-sectional area (S). r_1 and r_2 are evolved by dr_{oc} , dr_v , dr_e , dr_f , and
22 dr_i (open channel melting, viscous deformation, elastic deformation, refreezing, and turbulent melting, respectively; colored as in Fig. 1). u_d
23 shears the moulin as prescribed by Glen's Flow Law. Ice thickness and subglacial path length are indicated by H_i and L , respectively. Ice
24 flow is from left to right. Further details are in Sect. 2. Modified from Trunz (2021). (b) WorldView-2 scene from July 2010 of an
25 approximately 1.2×0.8 km region surrounding the example moulin (yellow) formed by a drained supraglacial lake. (c) Detail of panel b,
26 with the inflow stream and moulin indicated. (d) Detail of panel c, showing the moulin minor radius r_1 , major radius r_2 , and water input Q_{in}
27 from the inflow stream, as represented in the MouSh model. Maps generated by authors. WorldView image © 2010 DigitalGlobe, Inc.



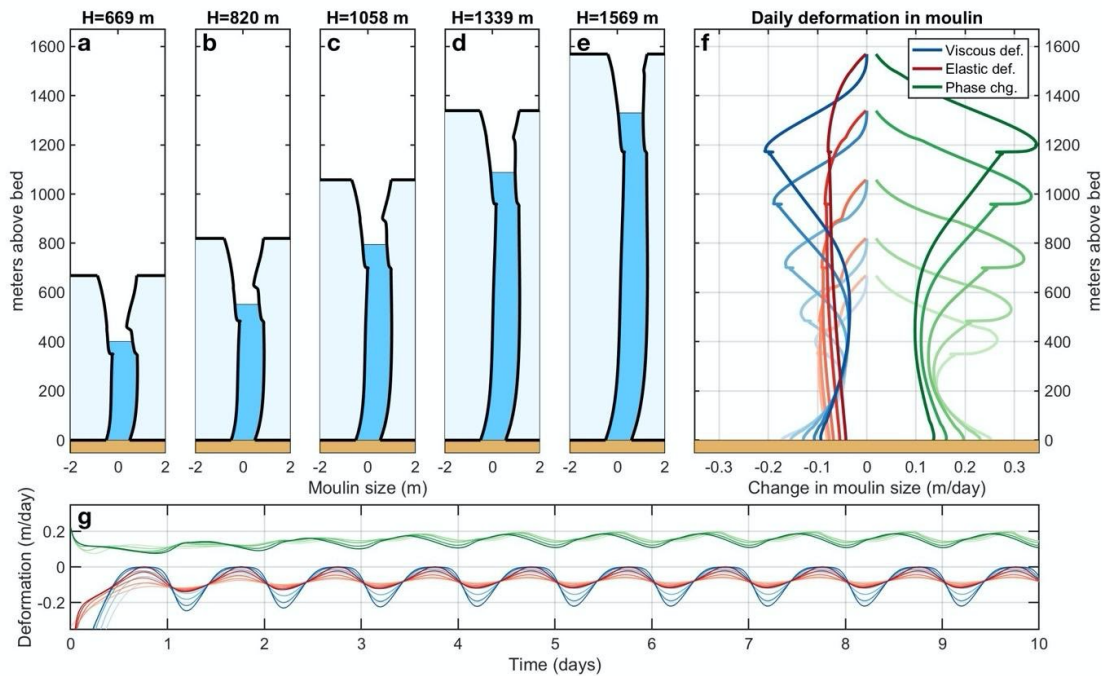
29

30 **Figure 3. Results of parameter sensitivity studies for 10-day MouSh model runs.** Shown are the sensitivity of moulin size to initial
 31 condition for moulin radius (a–b), enhancement factor for englacial ice (c–d), ice temperature scenario (e–f), Young’s modulus (g–h), softness
 32 of basal ice (i–j), friction factor for water flow beneath the water line (k–l), friction factor for water flow above the water line (m–n), and ice
 33 thickness (o–p). The left column shows the moulin radii (black and grey) at the mean water level and the mean subglacial channel radius
 34 (purple) averaged over the final 24-hour period of the ten-day model run. The right column shows the equilibrium water level (blue), moulin
 35 volume (red), and volume of water in the moulin (gold) averaged over the same 24-hour period. Overall, moulin radius is most sensitive to
 36 the friction factors, while moulin water level and volume are most sensitive to ice thickness H_i and basal ice softness A .

37



39
40
41 **Figure 4. Diurnal variations in moulin sizes in 10-day parameter sensitivity runs.** Shown are the sensitivity of diurnal variation in
42 moulin size and water storage metrics to initial condition for moulin radius (a–b), enhancement factor for englacial ice (c–d), ice temperature
43 scenario from coldest to warmest ice (e–f), Young's modulus (g–h), softness of basal ice (i–j), friction factor for water flow beneath the water
44 line (k–l), friction factor for water flow above the water line (m–n), and ice thickness (o–p). The left column shows diurnal variations in
45 moulin radii (black and grey) at the equilibrium water level and the subglacial channel radius (purple) in the final 24-hour period of the ten-
46 day model run. The right column shows the diurnal variation in water level (blue), moulin volume (red), and volume of water in the moulin
47 (gold) within the same 24-hour period.



50

51

52 **Figure 5. Contributions of viscous deformation, elastic deformation, and phase changes to moulin geometry.** (a–e) Equilibrium
53 geometries of five moulins in ice of different ice thicknesses H (same as Fig. 6o–p) averaged over the final 24-hour period of a 10-day model
54 run. (f) Vertical variation of viscous deformation (blue), elastic deformation (red), and phase change (green) contributions to moulin
55 geometry averaged over the same 24-hour period. Negative values indicate contributions to moulin closure; positive values open the
56 moulin. Darkening shades of each color map to moulins of increasing ice thickness. Closure and opening rates are greatest at the minimum
57 daily water level (which is inferable by the lower notch in the moulin wall). (g) Time series of the components shown in panel f (colors the
58 same) at the mean water level over the entire ten-day model run. The greater diurnal range in water level in moulins in thick ice drives the
59 observed larger diurnal variations in viscous and elastic deformation.

60

61

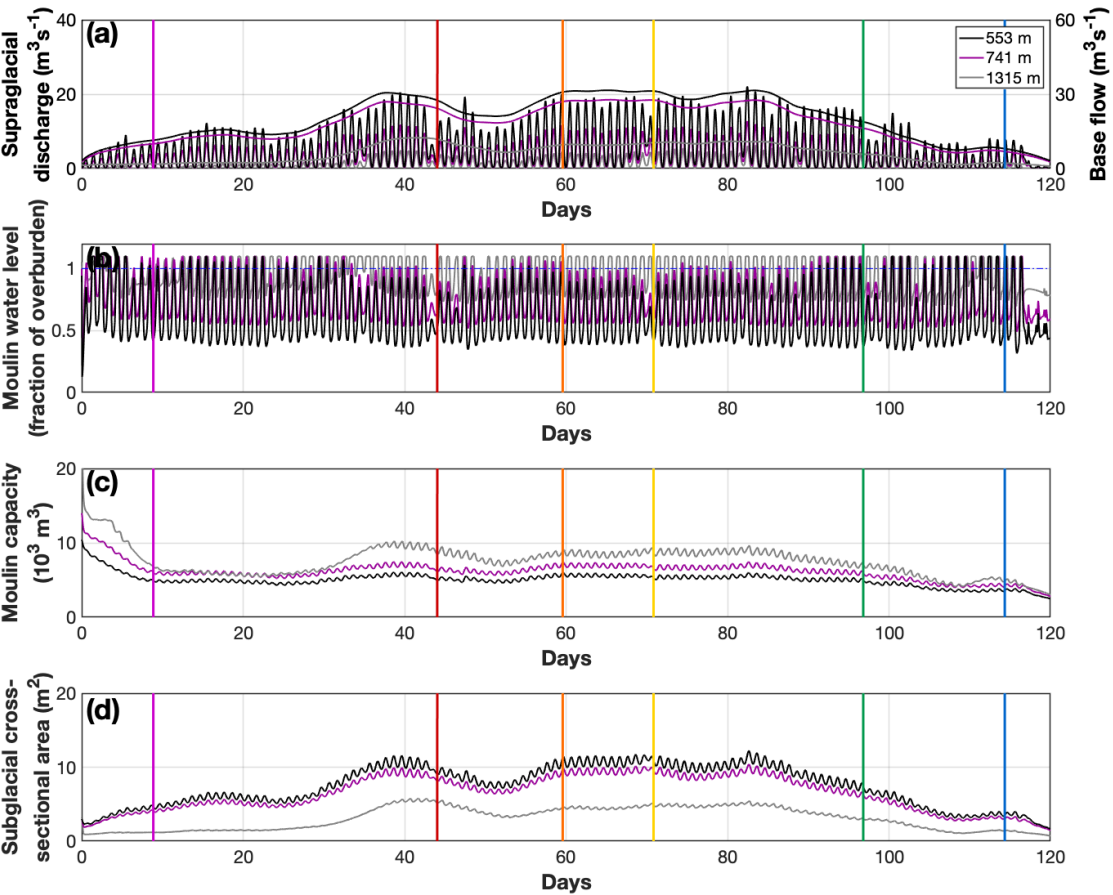
62

63

64

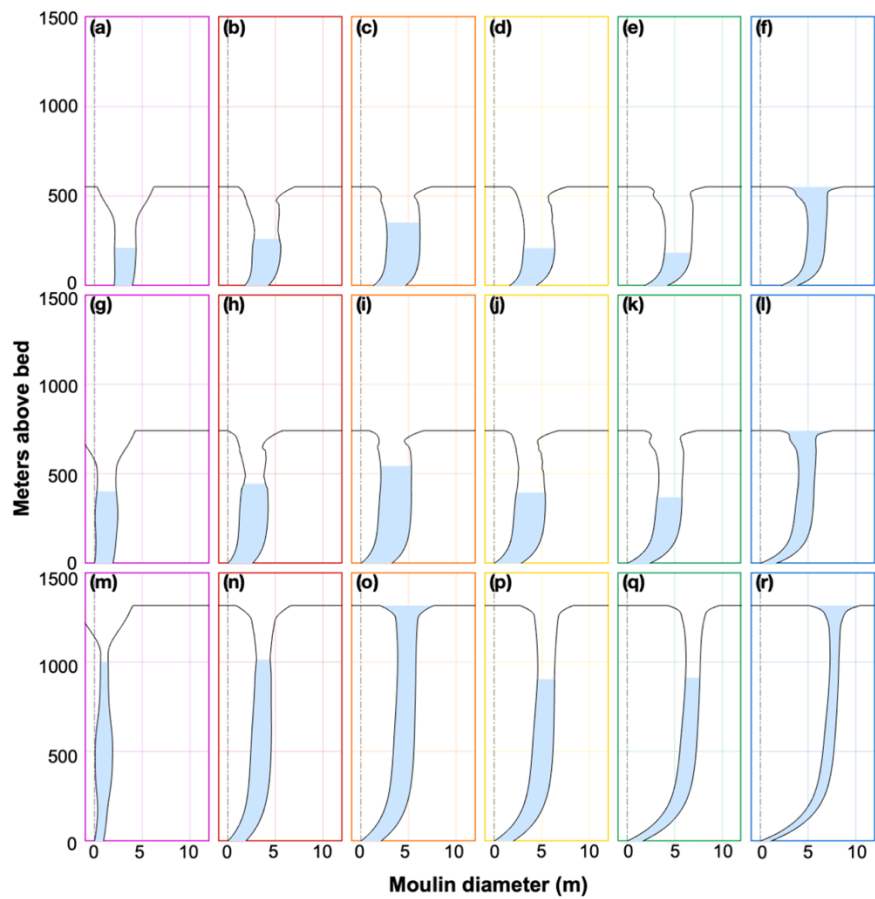
65

66



68
69 **Figure 6. MouSh model runs with realistic supraglacial and ice conditions.** The model runs are for a low-elevation basin (553 m ice
70 thickness; black lines), mid-elevation basin (741 m ice thickness; purple lines), and high-elevation basin (1315 m ice thickness; grey lines).
71 (a) Supraglacial discharge into the moulin Q_{in} and prescribed base flow Q_{base} . (b) Moulin water level as a fraction of overburden. Note that
72 the highest elevation moulin exceeds the ice surface most days. (c) Moulin capacity, or the total moulin volume. (d) Subglacial channel
73 cross-sectional area. Colored vertical lines indicate times in Fig. 7.

79 Figure 7



80

81 **Figure 7. Evolution of moulin geometry over the melt season.** Colored boxes correspond to the times indicated in Fig. 6. (a–f) Basin 1
82 with ice thickness of 553 m. (g–l) Basin 2 with ice thickness of 741 m. (m–r) Basin 3 with ice thickness of 1315 m. Axes are not to scale.

83

84

85

86

87

88
89
90
91
92
93
94
95
96
97
98
99
00
01
02
03
04
05
06
07

Figure 8

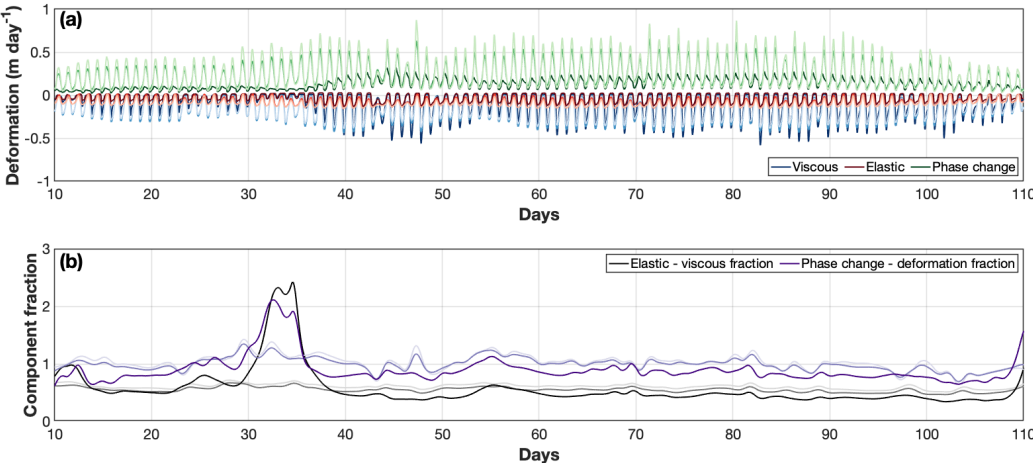


Figure 8. Time series of viscous, elastic and phase change components of moulin evolution and their relative importance in determining moulin geometry. (a) Time varying viscous (blues), elastic (reds), and phase change (melting, greens) components of moulin geometry. (b) The ratio of elastic to viscous deformation (greys) indicates the relative importance of the two deformational processes in moulin evolution. All values are lower than 1, indicating that viscous deformation is always greater. The ratio of the total amount of phase change (melting above and below the water line) to total deformation (elastic plus viscous; purples). Values above 1 indicate that melting dominates; values below 1 indicate that deformation dominates. Data is smoothed over 24 h. For both panels, light colors are for Basin 1 ($H_i=553$ m), medium colors for Basin 2 ($H_i=741$ m), and dark colors for Basin 3 ($H_i=1315$ m).

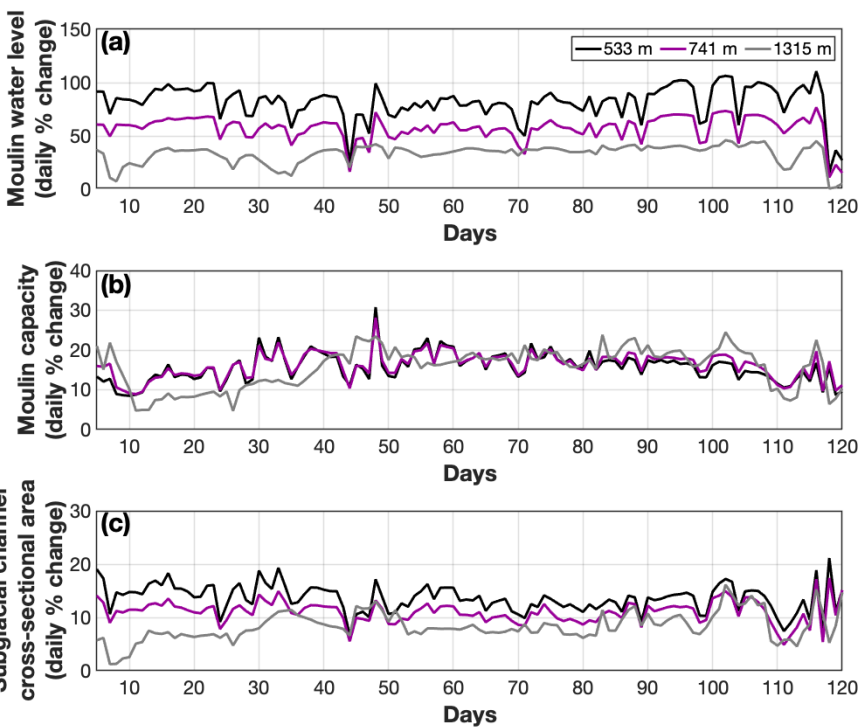
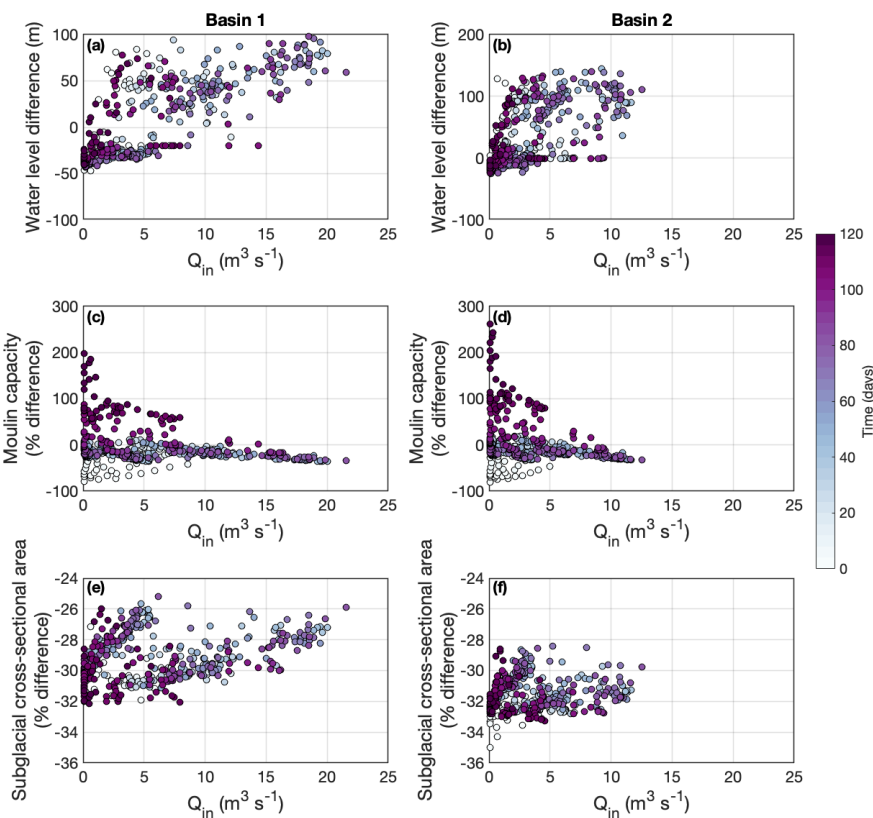


Figure 9. Daily percentage change in moulin variables relative to the daily mean value. (a) Daily percentage change in moulin water level relative to the daily mean water level for Basins 1, 2, and 3 (black, purple, and grey lines, respectively). (b) Daily percentage change in moulin capacity relative to the daily mean moulin capacity. (c) Daily percentage change in the subglacial channel cross-sectional area relative to the daily mean value. For (b–c), colors are as in (a).



24
25 **Figure 10. Difference between variable and fixed moulin geometries for Basin 1 and 2** (ice thicknesses of 553 m and 741 m,
26 respectively). The fixed moulins are cylinders with a fixed radius of 1.4 m (Basin 1) and 2 m (Basin 2), which are the time-mean radius at
27 the equilibrium water level for the variable moulins. In all instances, the difference is calculated as (*cylindrical* – *variable*) with instances of
28 percentage difference calculated as (*cylindrical* – *variable*) / (*variable*). (a, b) Difference in moulin water level for Basin 1 (black) and Basin
29 2 (purple). Negative values indicate periods where the variable moulin water levels are higher than those of the fixed cylindrical moulin. (c,
30 d) Percentage difference in moulin capacity. When values are negative, the variable moulin is larger than the fixed cylindrical moulin. (e,
31 f) Percentage difference in subglacial channel cross-sectional area. These values are persistently negative, indicating that the subglacial
32 channel is larger with a variable moulin.

33

34

35 **Table 1. MouSh model constants and parameter ranges.** During realistic runs (Sect. 2.4) Median values were generally
36 used. In instances where values used differ from the median value, the values used is indicated in parentheses.

Constant		Value		Units
ρ_i	Ice density	910		kg m ⁻³
ρ_w	Water density	1000		kg m ⁻³
g	Gravitational acceleration	9.81		m s ⁻²
L_f	Latent heat of fusion	335000		J kg ⁻¹
M_u	Dynamic viscosity (liquid water)	0.0017916		Pa s
K_w	Thermal conductivity (liquid water)	0.555		J (m K s) ⁻¹
C_w	Heat capacity (liquid water)	4210		J (K kg) ⁻¹
C_p	Heat capacity (ice)	2115		J (K kg) ⁻¹
Parameter		Median value	Range	Units
R ₀	Initial moulin radius	2.4 (3)	0.5 to 5	m
E	Ice deformation enhancement factor	5	1 to 9	-
T(z)	Ice temperature	-6 (FOXX profile)	-23 to 0	°C
Y	Young's modulus	5 (9)	1 to 9	GPa
A	Basal ice softness	6 x 10 ⁻²⁴	5 x 10 ⁻²⁵ to 5 x 10 ⁻²³	Pa ⁻³ s ⁻¹
f _M	Friction factor (under water)	0.1	0.01 to 1	-
f _{OC}	Friction factor (subaerial / open channel)	1 (0.8)	0.01 to 1	-
H	Ice thickness	1058 (553, 741, 1315)	669 to 1569	m

37

38

39 **Table 2. General ice and moulin input parameters for realistic runs**

Parameter	Basin 1	Basin 2	Basin 3
Ice thickness (m)	553	741	1315
Distance from terminus (km)	13.6	24.5	77.1
Catchment size (km ²)	19.8	18.4	55.5
Moulin input, mean diurnal range (m·s ⁻³)	11.5	6.7	2.5
Moulin input, maximum value (m·s ⁻³)	22.1	12.8	6.3
Baseflow, mean value (m·s ⁻³)	20.2	21.2	6.2

40